



Fluid–rock interactions in CO₂-saturated, granite-hosted geothermal systems: Implications for natural and engineered systems from geochemical experiments and models

Caroline Lo Ré^{a,*}, John P. Kaszuba^{a,b}, Joseph N. Moore^c, Brian J. McPherson^c

^a Department of Geology and Geophysics, 1000 E. University Avenue, University of Wyoming, Laramie, WY 82071, USA

^b School of Energy Resources, 1000 E. University Avenue, University of Wyoming, Laramie, WY 82071, USA

^c Energy and Geoscience Institute, University of Utah, 423 Wakara Way, Suite 300, Salt Lake City, UT 84108, USA

Received 18 November 2013; accepted in revised form 16 June 2014; Available online 27 June 2014

Abstract

Hydrothermal experiments were conducted and geochemical models constructed to evaluate the geochemical and mineralogical response of fractured granite and granite + epidote in contact with thermal water, with and without supercritical CO₂, at 250 °C and 25–45 MPa. Illite ± smectite ± zeolite(?) precipitate as secondary minerals at the expense of K-feldspar, oligoclase, and epidote. Illite precipitates in experiments reacting granite and granite + epidote with water; metastable smectite forms in the experiments injected with supercritical CO₂. Waters are supersaturated with respect to quartz and saturated with respect to chalcedony in CO₂-charged experiments, but neither mineral formed. Carbonate formation is predicted for experiments injected with supercritical CO₂, but carbonate only formed during cooling and degassing of the granite + epidote + CO₂ experiment.

Experimental results provide insight into the buffering capacity of granites as well as the drivers of clay formation. Metastable smectite in the experiments is attributed to high water–rock ratios, high silica activities, and high CO₂ and magnesium–iron concentrations. Smectite precipitation in supercritical CO₂-bearing geothermal systems may affect reservoir permeability. Silicate formation may create or thicken caps within or on the edges of geothermal reservoirs. Carbonate formation, as desired for carbon sequestration projects coinciding with geothermal systems, may require extended periods of time; cooling and degassing of CO₂-saturated waters leads to carbonate precipitation, potentially plugging near-surface production pathways. © 2014 Elsevier Ltd. All rights reserved.

1. INTRODUCTION

Shallow crustal rocks routinely undergo fluid–rock interactions driven by thermal, chemical, and/or physical disequilibrium. The resulting mass transfer has important implications for our understanding of processes such as hydrothermal alteration, ore formation, fault-zone permeability, and sedimentary diagenesis. Mass transfer is also especially important to geothermal operations since chemical reactions can impact production.

Our study comes at a time of renewed interest in conventional (convective) and non-conventional (conductive)

Abbreviations: scCO₂, supercritical CO₂; EGS, enhanced geothermal systems; CCS, carbon capture and storage; GWB, the Geochemist's Workbench; CPG, CO₂-plume geothermal systems.

* Corresponding author. Tel.: +1 307 766 3386; fax: +1 307 766 6679.

E-mail addresses: flore@uwyo.edu (C. Lo Ré), john.kaszuba@uwyo.edu (J.P. Kaszuba), jmoore@egi.utah.edu (J.N. Moore), b.j.mcperson@utah.edu (B.J. McPherson).

<http://dx.doi.org/10.1016/j.gca.2014.06.015>

0016-7037/© 2014 Elsevier Ltd. All rights reserved.

geothermal systems for energy extraction (e.g., Moore and Simmons, 2013) as well as for sequestering carbon dioxide to mitigate concentrations of atmospheric carbon (e.g., Benson and Cook, 2005). Water is the naturally occurring fluid in geothermal systems and is commonly used as the working fluid for heat extraction. Supercritical CO₂ (scCO₂) has also been proposed as a working fluid (Brown, 2000; Pruess, 2006). Non-conventional enhanced geothermal systems (EGS) (MIT, 2006) and conventional CO₂-plume geothermal systems (CPG) (Randolph and Saar, 2011) are both targets for using scCO₂ as a working fluid, with the possible ancillary benefit of sequestering carbon dioxide.

One goal of a CO₂-based geothermal system (whether EGS or CPG) is to dry out the reservoir over time by gradually extracting and displacing water. Another goal is to optimize heat extraction efficiency. The advantage of using scCO₂ compared to water is its low viscosity, large expansivity, and reduced reactivity with rock. In addition to increased productivity, scCO₂-based geothermal systems may sequester carbon, especially by mineral and/or dissolution trapping (Benson and Cook, 2005) or by loss to surrounding country rock if permeability is high enough.

CO₂-rich fluids, however, are chemically aggressive and could impact reservoir permeability and porosity by dissolution and precipitation reactions. Because there are few natural laboratories (CO₂ reservoirs) where the evolution of fluid and hydrothermal alteration can be assessed, we have used hydrothermal experiments and geochemical models to: (1) quantify fluid–rock interactions in granite-hosted hydrothermal systems, with and without scCO₂; and (2) bridge the gap that often exists among field observation, experimental results, and geochemical predictions. Our results elucidate processes such as the buffering capacity of felsic rocks, drivers of metastable clay formation, and tungsten ore formation. Results also clarify fluid–rock interactions in scCO₂-based EGS or CPG as well as in high temperature granitic or arkosic reservoirs targeted for carbon capture and storage (CCS).

Many experimental efforts have been made over the past 50 years to elucidate hydrothermal fluid–rock interactions for felsic igneous rocks, and all offer unique contributions to our understanding of natural and engineered systems (Appendix A). The associated batch and flow-through experiments were conducted at temperatures and pressures ranging from 20 to 600 °C and 1.4–150 MPa with distilled water, or less commonly, dilute Na–Cl, Na–HCO₃–Cl, or Na–Ca–HCO₃–Cl water. A few used scCO₂ at the onset of each experiment. To date, we are unaware of any studies using both scCO₂ and a realistic groundwater chemistry. We are also unaware of any that allow a system to approach a steady-state prior to introducing scCO₂. Our experiments were designed to explore such conditions.

A commonality observed in the referenced studies is the frequent precipitation of smectite as a secondary mineral. Based on our knowledge of natural systems, smectite and mixed-layer illite–smectite are characteristic of temperatures up to ~180 and ~220 °C, respectively (e.g., Henley and Ellis, 1983), and therefore, experimental observation of smectite formed at temperatures higher than ~180–

220 °C begs explanation. To our knowledge, this discrepancy is not discussed in the literature, and because of its critical implications for geothermal systems, we review and discuss the discrepancy in the context of experimental systems, geochemical models, and natural systems.

We present experimental data to evaluate aqueous geochemistry and mineralogical relationships in water–granite ± scCO₂ and water–epidote–granite ± scCO₂ systems at 250 °C and 25–45 MPa. Granite and epidote–granite experiments provide a baseline understanding for fluid–rock interactions in fresh and altered rock, respectively. We also construct thermodynamic models and compare calculations/predictions to our experimental results, and then compare our experimental and model data to natural and engineered systems. Although beyond the scope of this paper, a kinetic model is also under development. Important discussion topics include: (1) paths to equilibrium including the extent to which experiments approach equilibrium and the sequence of water–rock reactions; (2) results in the context of natural systems, including factors that govern smectite formation; and (3) implications for engineered systems.

2. METHODS AND MATERIALS

2.1. Experimental design and setup

Hydrothermal experiments were conducted in rocking autoclaves and flexible Au–Ti reaction cells (Dickson cells) (Seyfried et al., 1987). Each gold cell ports directly to a valve that allows for periodic fluid sampling without perturbing the experiment. Aqueous samples were collected approximately every 1, 2, 5, 14, and 28 days for each stage of an experiment (pre- or post- CO₂ injection). We also analyzed unreacted water and minerals (i.e., prepared for but not included in the experiment) as well as the very final reacted water and minerals (i.e., recovered at the conclusion of the experiment).

Our experiments and geochemical simulations emulate the geothermal conditions, aqueous geochemistry, and mineralogy of Roosevelt Hot Springs, Utah (Ward et al., 1978; Capuano and Cole, 1982), a well-characterized, magmatically-heated geothermal system. Basing simulations and experiments on such a system allows us to relate results to similar settings. With respect to CO₂-based EGS or CPG, our experiments are representative of conditions when the reservoir water is saturated with CO₂ and has not yet been displaced by scCO₂. Experiments have initial and final water:rock ratios of ~20:1 and 10:1, respectively; this emulates the high water:rock ratio in a localized zone of fractured granite.

The granite is a mixture of powdered (75%, <45 μm) and chipped (0.1–0.7 cm) research-grade quartz, plagioclase feldspar (oligoclase), potassium feldspar (K-feldspar), and minor biotite. Instead of using actual granite, this approach allowed us to avoid alteration and accessory minerals, thus simplifying analysis of our modeling and experimental results. Two experiments also include 50% epidote, and simulate fluid–rock interactions in EGS reservoirs stimulated by fracturing along pre-existing zones of weakness

(i.e., epidote veins) and in pervasively altered granitic rocks (i.e., propylitic or greenschist facies alteration). Proportions of minerals used in each experiment are listed in Table 1; the composition of each mineral is listed in Table 2.

A multi-component, but dominantly Na–Cl water was used in the experiments. The waters (ionic strength (I) ≈ 0.1 molal) were prepared using research-grade salts and solutions and contained molal quantities of Na, Cl, and HCO_3 and millimolal quantities of K, $\text{SiO}_2(\text{aq})$, SO_4 , Ca, Al, and Mg (initial compositions are shown in Table 3).

Five hydrothermal experiments were conducted: one water–granite experiment (EXP-1), two water–granite– scCO_2 experiments (EXP-2 and -3), one water–epidote–granite experiment (EXP-4) and one water–epidote–granite– scCO_2 experiment (EXP-5). EXP-2 and -3 are similar with the exception of initial pH, which we varied to observe the effect of pH on initial water–rock interactions (EXP-2 pH = 5.7; EXP-3 pH = 3.9). We refer to EXP-2 and -3 as moderate and low pH water–granite– scCO_2 experiments, respectively. Table 1 outlines conditions and parameters for each experiment. All experiments included an initial water–rock stage conducted at 250 °C and 25 MPa that lasted at least 666 h. Two of the experiments (EXP-1 and -4) were terminated when the aqueous chemistry approached a steady-state. Three of the experiments (EXP-2, -3, and -5) continued for at least another 650 h after injecting scCO_2 . The scCO_2 stage of these experiments continued at 250 °C with final pressures between 30.7 and 44.8 MPa. Final pressures stabilized over a period of 1–2 days as CO_2 dissolved into the water.

The amount of CO_2 injected into EXP-2, -3, and -5 ensured $\Sigma\text{CO}_2(\text{aq})$ saturation for the duration of each experiment. The Duan and Sun (2003) and/or Duan et al. (2006) equations of state for CO_2 were used to calculate

the target amounts of injected CO_2 . Based on mass balance data, excess scCO_2 was present in EXP-2 and -3 for the duration of each experiment. EXP-5 developed a leak 281 h after scCO_2 injection (363 h prior to termination). However, we believe $\Sigma\text{CO}_2(\text{aq})$ saturation was maintained throughout the experiment because we observed no abrupt changes in aqueous chemistry after detecting the leak. During sample collection before and after detection of the leak, we also observed a consistent volume of degassed CO_2 from the aqueous phase, further indicating saturation throughout the experiment.

2.2. Analytical methods

We analyzed filtered (0.45–0.5 μm) aqueous samples for major cations, major anions, and trace metals by inductively-coupled plasma optical emission spectroscopy (ICP-OES), ion chromatography (IC), and inductively-coupled plasma mass spectrometry (ICP-MS), respectively. pH was measured using an Orion pH meter and Ross micro-electrode. The samples for cation analysis were diluted approximately 10 \times and acidified with trace-metal-grade nitric acid.

We analyzed unreacted and reacted minerals and mineral digests using a combination of optical microscopy, X-ray diffraction (XRD) (Cu-K α), ICP-OES, ICP-MS, IC, electron microprobe, high-resolution field emission scanning electron microscopy (FE-SEM), and energy dispersive spectra (EDS). XRD analysis was performed on whole rock samples as well as clay separates. Surface areas of mineral powders were determined using the Brunauer, Emmett and Teller (BET) method (Brunauer et al., 1938). BET data are not discussed further, but are included in Tables 1 and 2.

Table 1
Experimental parameters and mineral compositions.

Experiment Description	EXP-1 Water + granite	EXP-2 Moderate pH water + granite + scCO_2	EXP-3 Low pH water + granite + scCO_2	EXP-4 Water + granite + epidote	EXP-5 Water + granite + epidote + scCO_2
Initial pH, Bench	5.6 \pm 0.1	5.7 \pm 0.1	3.9 \pm 0.1	5.1 \pm 0.1	5.2 \pm 0.1
Temperature (°C)	250.1 \pm 0.8	250.2 \pm 1.9	250 \pm 2.4	250.1 \pm 0.4	249.8 \pm 2.0
Pressure (MPa), Pre- scCO_2	25.3 \pm 0.7	25.0 \pm 1.0	25.2 \pm 0.7	24.9 \pm 0.8	25.2 \pm 0.7
Injection Pressure (MPa), Post- scCO_2	N/A	30.7 \pm 0.9	44.8 \pm 0.9	N/A	33.9 \pm 0.8
Initial water:rock ratio	19.4	20.0	19.0	20.0	20.4
Rock mass ^a	10.84	12.04	11.08	11.81	9.56
Mineral proportions (Qtz:Olg:Kfs:Bt:Ep) ^b	32:32:32:4:0	32:32:32:4:0	32:32:32:4:0	16:16:16:2:50	16:16:16:2:50
Water–rock reaction time (h)	1024	700	674	858	666
Water–rock– scCO_2 reaction time (h)	N/A	1027	1121	N/A	650
Total reaction time (h)	1024	1727	1795	858	1316
Surface area of reacted powders (m ² /g) ^c	0.7450 \pm 0.0009	0.5765 \pm 0.0316	1.0372 \pm 0.0062	2.6224 \pm 0.0089	3.1251 \pm 0.0323

DL = below detection limit, N/A = not applicable, sc = supercritical.

^a Rock mass input into reaction cell.

^b Quartz, oligoclase, K-feldspar, biotite, and epidote proportions.

^c Surface areas determined by BET.

Table 2
Mineral Compositions and Initial Surface Areas.

Component ^{a,b}	Quartz	K-feldspar	Oligoclase	Biotite	Epidote
<i>Elemental weight percent of mineral reactants (wt% oxide)</i>					
P ₂ O ₅	DL	DL	DL/NM	DL/NM	DL
MnO	DL	0.00	0.01/DL	1.03/0.87	0.09
Fe ₂ O ₃	0.08	0.19	0.12/0.04	22.84 ^a	12.81
FeO	–	–	–	17.65 ^b	–
MgO	DL	DL	DL/DL	13.78/13.82	DL
SiO ₂	97.79	62.48	64.29/61.83	36.17/38.21	34.70
Al ₂ O ₃	0.59	18.92	24.47/24.25	11.56/11.33	22.63
CaO	DL	0.22	5.23/4.65	0.10/0.01	23.69
TiO ₂	0.03	0.01	0.02/DL	2.50/2.12	0.12
Na ₂ O	DL	2.35	8.36/8.67	0.60/0.43	DL
K ₂ O	DL	12.60	0.71/0.50	8.93/9.37	DL
F	NM	NM	NM/DL	NM/2.57	NM
Cl	NM	NM	NM/DL	NM/0.04	NM
Total	98.48	96.86	103.37/99.94	97.50/96.44	94.04
Mineral formula	SiO ₂	25% NaAlSi ₃ O ₈ 75% KAlSi ₃ O ₈	Na _{0.77} Ca _{0.23} (Si _{2.77} ,Al _{1.23})O ₈	K(Mg _{1.7} ,Fe _{1.3}) (AlSi ₃ O ₁₀)(OH) ₂	Ca ₂ (Al _{0.2} Fe _{0.8}) Al ₂ Si ₃ O ₁₂ (OH)
Source	Unknown	Unknown	Mitchell County, North Carolina	Ontario, Canada	Unknown
<i>Surface Area of Unreacted Powders (m²/g)^c</i>					
EXP-1	0.3367 ± 0.0028	0.4408 ± 0.0208	0.6303 ± 0.0070	1.5652 ± 0.0420	N/A
EXP-2	0.3367 ± 0.0028	0.927 ± 0.0385	0.6303 ± 0.0070	1.5652 ± 0.0420	N/A
EXP-3	0.3367 ± 0.0028	0.4408 ± 0.0208	0.6303 ± 0.0070	1.5652 ± 0.0420	N/A
EXP-4	0.7124 ± 0.0031	0.927 ± 0.0385	0.6303 ± 0.0070	1.5652 ± 0.0420	0.6327 ± 0.0617
EXP-5	0.7124 ± 0.0031	0.927 ± 0.0385	0.6303 ± 0.0070	1.5652 ± 0.0420	0.6327 ± 0.0617

DL = below detection limit, N/A = not applicable, NM = not measured.

^a Component analysis conducted by ICP-OES after acid digestion of mineral.

^b Component analysis for oligoclase and biotite also conducted by electron microprobe. Microprobe data are the second set of values shown.

^c Surface areas determined by BET. Powders comprise 75% of mineral reactants with the remaining 25% consisting of mineral chips.

2.3. Geochemical calculations

Geochemical models were developed using The Geochemist's Workbench[®] version 8.0.10 (GWB) (Bethke and Yeakel, 2009), the b-dot ion association model, and the resident thermodynamic database thermo.dat. We use the b-dot model because CO₂(aq) is predominantly H₂CO₃(aq) (>99%) and low ionic strengths (0.10–0.15) prevail in our CO₂-charged experiments. We also assume that effects of CO₂ on mineral solubility are due to the pH effect (see also Lu et al., 2013). We use thermo.dat because it is internally consistent and handles aluminum speciation more adeptly than other available databases (e.g., Kaszuba et al., 2011). The models were used to: (1) determine initial water compositions used in the experiments; (2) calculate in situ pH conditions, aqueous species concentrations and activities, and mineral stabilities for individual aqueous samples periodically collected from each experiment; and (3) predict activities of aqueous species and mineral stabilities at equilibrium in each of the experiments.

To provide a better representation of thermodynamic data for minerals used in our experiments, we adjusted the database to include solid–solution plagioclase and epidote with equilibrium constants calculated via ideal solution models. Biotite was treated as a mechanical mixture of 44% annite and 56% phlogopite. The K-feldspar is

perthitic, and was treated as a mechanical mixture of 25% albite and 75% microcline.

GWB was used to determine a water chemistry that would be as close to equilibrium as possible with the minerals in each experiment. This was done to minimize water–rock interaction in the experiments prior to injecting scCO₂.

In situ pH was calculated for samples in the water–rock segment of each experiment by speciating the fluid at 250 °C using bench pH, ΣCO₂(aq) measured at the bench and in situ, and the aqueous geochemical data (Table 3). For those experiments injected with scCO₂, in situ pH was calculated using the method of Newell et al. (2008) by speciating the fluid using pH and ΣCO₂(aq) measured at the bench, the aqueous geochemical data, and ΣCO₂(aq) calculated for in situ conditions. Aqueous species activities from these calculations are plotted on activity–activity diagrams to better define the sequence of water–rock reactions for each experiment (Section 4.1).

Equilibrium models were constructed to predict activities and concentrations of aqueous species and secondary mineral assemblages for each experiment both before and after injection of scCO₂. Each model incorporates the fluid–rock proportions, mineralogy, and aqueous geochemistry of each experiment (Tables 1–3). The model predicts the geochemical behavior of the water–rock segment of each experiment (i.e., the entirety of EXP-1 and -4 and

the first half of EXP-2, -3, and -5), by speciating the fluid and dissolving and precipitating minerals at 250 °C. For those experiments injected with scCO_2 (EXP-2, -3, and -5), an appropriate amount of $\Sigma\text{CO}_2(\text{aq})$ was titrated into each system, as calculated using the [Duan and Sun \(2003\)](#) equation of state (Section 3.4). The resulting predicted aqueous concentrations are included in [Table 3](#) and on [Fig. 1](#) in the column labeled 'P' (i.e., 'predicted') on the right side of each graph. Predicted, observed, and typical field alteration mineralogy is outlined in [Table 4](#).

3. EXPERIMENTAL AND THEORETICAL RESULTS

3.1. Mineral precipitation

Mineral precipitation occurred in all five experiments ([Table 4](#)). XRD results for whole rock samples do not exhibit discernible diffractograms for secondary minerals. However, clay fraction diffractograms ([Fig. 2](#)) and optical/SEM observation (below) do indicate clay precipitation in each experiment. Both air-dried and glycolated clay-fraction samples were analyzed; for brevity, air-dried results are not contained herein.

XRD results for unreacted and reacted powders (EXP-1, -2, and -3) indicate the presence of illite. Illite may also be present in the reacted epidote–granite powders (EXP-4 and -5), although the diffraction peaks are not well defined. Based on optical and SEM observation, minimal illite occurs in the unreacted granite as compared to reacted granite suggesting additional illite precipitated in the experiments. XRD results also indicate the presence of smectite in the water–granite– scCO_2 experiments (EXP-2 and -3) and the water–epidote–granite– scCO_2 experiment (EXP-5). Although XRD data are insufficient to identify the types of illite and smectite, we are confident that the clays are not interlayered due to the lack of characteristic peaks for regularly or randomly interlayered illite–smectite.

We observed three precipitates in the water–granite experiment (EXP-1) including a sparse needle-forming aluminosilicate (zeolite?) (e.g., [Fig. 3a](#)), an abundant petal-forming Mg–Fe-rich aluminosilicate interpreted as illite (possibly celadonite) ([Fig. 3b](#)), and one occurrence of hummocky silica. The illite is zoned in reflected light and varies from green to blue. The silica is interpreted to have deposited during cooling (Section 3.3).

In the water–granite– scCO_2 experiments (EXP-2 and -3), we observed similarly composed illite and zeolite(?) in addition to an Fe–Mg-rich, rosette-forming aluminosilicate interpreted as smectite ([Fig. 3c](#)). The low pH water–granite– scCO_2 experiment (EXP-3) contains minor amounts of three additional minerals, as identified by EDS: scheelite (CaWO_4), magnetite, and gold ([Fig. 3d–f](#)).

The water–epidote–granite experiment (EXP-4) contained trapezohedral analcime, petal-forming illite (Fe–Ca rich), and rosette-forming smectite (Fe–Mg rich) ([Fig. 3g–i](#)). Smectite is a minor phase since only one occurrence was observed during optical and SEM analysis and there is no evident XRD peak.

In the water–epidote–granite– scCO_2 experiment (EXP-5), abundant, poorly-formed smectite (Fe–Ca-rich)

([Fig. 3j](#)), blocky and rhombohedral Ca-carbonate, ([Fig. 3k and l](#)), and globular silica formed. Based on XRD data, illite is also likely present ([Fig. 2](#)), but could not be positively identified by SEM. Based on aqueous geochemistry and saturation indices (not shown), the carbonate and silica formed as an artifact of terminating the experiment (Section 3.3). The presence of carbonate may be specific to EXP-5 due to abundant calcium from epidote dissolution. Although only observed in EXP-1 and -5, silica may have formed on termination of the other experiments as well. We made no effort to identify the type of silica that precipitated since it does not relate to in situ experimental conditions.

The tungsten source in EXP-3 is likely high-temperature lubricant. In addition, we attribute gold precipitation to mobilization from the reaction cell during the experiment; the morphology of the gold crystals indicates precipitation from solution and not contamination from sample coating or abrasion of the reaction cell.

3.2. Mineral dissolution

Minerals from the water–rock– scCO_2 experiments (EXP-2, -3, and -5) display a greater degree of dissolution than minerals in the water–rock experiments (EXP-1 and -4). The feldspars in the water–granite experiments (EXP-1, -2, and -3) exhibit dissolution textures ([Fig. 4a–d](#)), with relatively more dissolution of K-feldspar than plagioclase. Feldspars in EXP-2 (initial pH = 5.7) are less dissolved than feldspars in EXP-3 (initial pH = 3.9). In the epidote–granite experiments (EXP-4 and -5), epidote ([Fig. 4e and f](#)), oligoclase ([Fig. 4g](#)), K-feldspar, and quartz ([Fig. 4h](#)) all exhibit dissolution textures, in order of decreasing extent. In all experiments, biotite appears fresh although clay has formed directly on some surfaces ([Fig. 4i](#)).

3.3. Major element aqueous geochemistry

[Table 3](#) presents aqueous geochemical data for each experiment, and [Fig. 1](#) shows select geochemical trends for EXP-1, -2, -4, and -5. Data from EXP-3 are not shown since results are generally similar to those from EXP-2.

The changes in cation and anion concentrations in each experiment over time indicate active fluid–rock interactions. The water–granite experiment (EXP-1) and the pre-injection stage of the water–granite– scCO_2 experiments (EXP-2 and -3) display relatively constant concentrations of Cl, Na, K, and SO_4 , increasing concentrations of $\text{SiO}_2(\text{aq})$ and Al, and decreasing concentrations of Mg ([Fig. 1a and b](#)). Concentrations for these analytes approach steady state at the termination of EXP-1 and prior to injecting scCO_2 into EXP-2 and -3. Calcium concentrations decrease and increase irregularly over time, suggesting that steady state was not established between the fluid and one or more calcium-bearing mineral(s).

Post-injection concentrations of Cl, Na, and K are relatively constant for EXP-2 ([Fig. 1b](#)) and EXP-3. Concentrations of Ca, SO_4 , and Al appear to decrease in both experiments during the first 5 days after scCO_2 injection while Mg concentrations increase over the same period of

Table 3
Aqueous geochemistry for all experiments, including analyzed and predicted concentrations.

Time (h)	pH (bench) ^a	pH (in situ) ^b	F	Cl	SO ₄	Na	K	Ca	Mg	Fe	SiO ₂ (aq)	Al	Mn	ΣCO ₂ ^f , bench	ΣCO ₂ ^{g,h} , in situ	Charge balance ⁱ (%)
<i>EXP-1: water chemistry (mmollkg), water + granite experiment</i>																
Initial water ^c	5.6 ± 0.1	6.4	0.01	161	0.81	130	8.8	1.0	0.8	<0.00002	3.4	0.0022	0.00012	0.10	0.10	−6.6
25.1	5.7 ± 0.1	6.6	0.04	161	0.87	135	9.7	1.4	0.3	<0.00002	6.0	0.0063	0.00191	0.10	0.10	−4.5
41.5	5.4 ± 0.1	6.6	0.05	158	0.85	129	9.4	1.5	0.2	<0.00002	6.8	0.0049	0.00080	0.34	0.34	−6.0
113.5	5.6 ± 0.1	6.5	0.05	158	0.78	130	8.3	1.6	0.2	<0.00002	7.4	0.0085	0.00066	0.11	0.11	−5.7
354.0	5.6 ± 0.1	6.5	0.06	157	0.75	130	9.1	1.7	0.2	<0.00002	7.6	0.0091	0.00037	0.16	0.16	−5.0
640.9	5.4 ± 0.4	6.5	0.02	149	0.69	135	8.2	1.5	0.2	<0.00002	8.3	0.0061	0.00076	0.46	0.46	−1.5
1023.6	5.5 ± 0.4	6.4	0.05	161	0.70	128	9.4	4.9	0.3	<0.00002	8.1	0.0066	0.00286	0.27	0.27	−4.7
Quench ^d	5.1 ± 0.1	5.1	0.04	148	0.71	122	8.2	1.8	0.2	<0.00002	7.5	0.0081	0.00378	0.02	0.02	−5.5
Uncertainty ± 1Σ ^j	–	–	0.02	10	0.04	4	0.4	0.3	0.1	–	0.5	0.0006	0.00007	±3.0%	–	–
Predicted equilibrium value ^e	–	6.2	–	142	0.64	132	10.3	0.1	0.001	0.005	6.2	0.003	–	–	0.1	–
<i>EXP-2: water chemistry (mmollkg), moderate pH water + granite + scCO₂ experiment</i>																
Initial water ^c	5.7 ± 0.1	6.4	0.01	149	0.73	123	8.9	1.4	0.7	<0.00002	3.6	0.0019	0.00013	0.10	0.10	−5.3
22.6	6.0 ± 0.2	6.7	0.01	137	0.62	123	8.1	1.8	0.2	<0.00002	5.8	0.0036	0.00061	0.56	0.56	−1.3
49.9	5.4 ± 0.1	6.5	0.04	140	0.67	127	10.7	2.4	0.2	<0.00002	6.7	0.0038	0.00078	0.65	0.65	0.5
117.9	5.3 ± 0.1	6.5	0.04	137	0.74	132	9.4	1.6	0.1	<0.00002	7.6	0.0057	0.00079	0.49	0.49	2.1
356.7	5.5 ± 0.3	6.5	0.03	136	0.53	130	8.9	1.8	0.2	<0.00002	7.7	0.0044	0.00062	0.57	0.57	2.2
693.0	5.4 ± 0.1	6.5	0.02	137	0.68	131	8.9	1.2	0.2	<0.0004	8.6	0.0064	0.00122	0.36	0.36	1.5
700.3, inject scCO ₂																
718.2	5.2 ± 0.2	4.3	0.02	135	0.45	134	9.1	1.1	0.5	<0.0004	9.0	0.0069	0.01281	13.35	2406	3.1
742.3	5.2 ± 0.1	4.4	0.02	137	0.37	131	9.2	0.9	0.6	<0.0004	8.8	0.0033	0.01095	15.44	2405	1.3
814.8	5.2 ± 0.1	4.4	0.02	136	0.39	135	8.9	0.9	0.6	<0.0004	9.3	0.0009	0.00741	15.34	2406	3.0
1053.7	5.3 ± 0.1	4.4	0.02	137	0.28	136	10.7	1.0	0.6	<0.0004	8.7	0.0007	0.00640	14.29	2404	3.6
1318.6	5.6 ± 0.1	4.7	0.02	137	0.30	134	10.3	1.1	0.5	<0.0004	8.2	0.0004	0.00525	17.76	2405	2.4
1726.5	5.3 ± 0.1	4.4	0.02	125	0.19	129	10.6	1.8	0.7	<0.0001	7.5	0.0008	0.00424	19.24	2414	6.3
Quench ^d	6.1 ± 0.3	6.3	0.03	126	0.92	130	9.7	2.5	0.7	<0.0001	7.3	0.0018	0.00861	6.83	–	5.2
Uncertainty ± 1Σ ^j	–	–	0.02	10	0.04	4	0.4	0.3	0.1	–	0.5	0.0006	0.00007	±3.0%	–	–
Predicted equilibrium value ^e , pre-injection	–	6.2	–	136	0.65	126	9.8	0.1	0.001	0.004	6.2	0.003	–	–	0.1	–
Predicted equilibrium value ^e , Post-Injection	–	5.9	–	136	0.74	186	10.9	0.1	0.007	0.009	6.1	0.002	–	–	2380	–
<i>EXP-3: water chemistry (mmollkg), low pH water + granite + scCO₂ experiment</i>																
Initial water ^c	3.9 ± 0.1	6.1	0.00	135	0.72	135	9.4	0.7	0.6	<0.00002	3.6	<0.00001	0.00026	0.10	0.10	3.8
22.4	3.1 ± 0.1	3.9	0.03	134	0.75	132	10.0	1.0	0.2	0.004	6.7	0.0010	0.00086	0.41	0.41	3.3
47.0	3.1 ± 0.1	3.9	0.02	133	0.73	133	6.6	1.0	0.2	<0.00002	7.5	0.0019	0.00062	0.42	0.42	2.5
114.5	3.0 ± 0.1	3.5	<0.001	133	0.73	132	9.1	1.1	0.2	<0.00002	8.1	<0.00001	0.00080	0.61	0.61	3.0
331.6	3.7 ± 0.2	6.0	0.03	139	0.80	131	8.5	3.6	0.3	<0.0003	8.3	0.0041	0.00135	0.30	0.30	2.5
667.9	5.4 ± 0.1	6.5	0.03	137	0.80	129	8.1	1.6	0.3	<0.0003	8.4	0.0048	0.00195	0.41	0.41	1.4
674, inject scCO ₂																
696.0	5.7 ± 0.1	3.9	0.04	143	0.61	134	8.5	1.5	0.7	<0.0003	8.8	0.0050	0.01128	0.67	3364	0.5
716.4	5.1 ± 0.1	4.1	0.03	138	0.50	129	8.7	1.3	0.6	<0.0003	8.6	0.0035	0.00755	13.15	3372	0.9
790.8	5.3 ± 0.1	4.3	0.03	135	0.42	136	9.0	1.3	0.7	<0.0003	8.5	0.0009	0.00551	17.15	3375	4.0
1001.7	5.5 ± 0.1	4.4	0.03	133	0.30	123	8.2	1.4	NI	<0.001	8.1	NI	0.04206	16.01	3378	4.2

1794.9	5.7 ± 0.1	4.7	0.02	163	0.31	138	10.0	1.6	0.6	<0.00002	6.8	0.0010	0.00379	23.23	3371	−5.3
Quench ^d	6.1 ± 0.1	6.4	0.02	156	1.06	136	9.2	2.4	0.7	<0.00002	6.7	0.0049	0.01289	5.75	–	−3.1
Uncertainty ± 1Σ ^j	–	–	0.02	10	0.04	4	0.4	0.3	0.1	–	0.5	0.0006	0.00007	±3.0%	–	–
Predicted equilibrium value ^e , pre-injection	–	6.2	–	147	0.63	137	10.6	0.1	0.002	0.005	6.2	0.003	–	–	0.1	–
predicted equilibrium value ^e , post-injection	–	5.8	–	147	0.73	198	11.4	0.1	0.001	0.01	6.1	0.002	–	–	3330	–
<i>EXP-4: water chemistry (mmollkg), water + granite + epidote experiment</i>																
Initial water ^c	5.1 ± 0.1	6.6	<0.001	135	0.66	122	7.9	0.67	0.007	<0.0001	5.5	0.015	0.00006	0.05	0.05	−1.9
22.1	5.8 ± 0.1	–	0.012	141	0.70	NI	NI	NI	0.032	NI	NI	0.063	0.00015	0.34	0.34	–
65.8	5.9 ± 0.1	6.8	0.014	140	0.69	123	7.7	1.41	0.002	<0.0001	8.4	0.011	0.00006	0.68	0.68	−2.7
139.3	5.8 ± 0.1	6.7	0.017	141	0.63	126	7.6	1.58	0.005	<0.0001	8.4	0.011	0.00009	0.76	0.76	−2.1
353.7	5.7 ± 0.1	6.7	0.023	138	0.55	122	7.0	1.63	0.006	<0.0001	8.3	0.008	0.00008	0.65	0.65	−2.6
858.2	5.6 ± 0.1	6.6	<0.001	139	0.51	127	7.3	1.56	0.008	<0.0001	8.1	0.009	0.00012	0.62	0.62	−1.0
Quench ^d	6.2 ± 0.2	6.2	0.011	139	0.69	121	7.1	1.87	0.016	<0.0001	7.8	0.010	0.00047	0.19	0.19	−3.2
Uncertainty ± 1Σ ^j	–	–	0.005	9	0.05	6	0.4	0.09	0.001	–	0.5	0.003	0.00001	±3.0%	–	–
Predicted equilibrium value ^e	–	7.2	–	131	0.67	122	9.5	0.10	2E-05	0.000007	6.3	0.003	–	–	0.05	–
<i>EXP-5: water chemistry (mmollkg), water + granite + epidote + scCO₂ experiment</i>																
Initial Water ^c	5.2 ± 0.1	6.5	0.007	119	0.61	129	7.7	<0.002	0.006	<0.0002	7.0	0.015	0.00004	0.05	0.05	6.0
21.1	6.1 ± 0.2	7.0	0.004	117	0.67	128	8.5	0.83	0.003	<0.0002	7.8	0.026	0.00027	1.03	1.03	7.3
47.8	6.2 ± 0.1	6.7	0.036	119	0.58	127	8.7	1.09	0.001	<0.0002	8.5	0.023	0.00013	0.19	0.19	6.8
115.6	6.1 ± 0.3	6.9	0.038	120	0.61	126	7.3	1.39	0.002	<0.0002	8.7	0.018	0.00016	0.68	0.68	5.4
330.1	5.9 ± 0.3	6.7	0.027	124	0.63	126	7.4	1.65	0.003	<0.0002	8.2	0.020	0.00016	0.49	0.49	4.6
666.4	5.9 ± 0.1	6.7	0.028	120	0.62	129	7.8	1.61	0.029	<0.0002	8.5	0.016	0.00019	0.63	0.63	7.3
672.1, Inject scCO ₂																
691.4	5.5 ± 0.2	4.5	0.014	121	0.17	129	5.4	2.22	0.187	<0.0002	8.9	0.004	0.00495	15.38	2650	5.8
716.7	5.3 ± 0.1	4.4	0.003	119	0.26	130	7.3	2.64	0.116	<0.0002	8.9	0.001	0.00488	19.60	2652	8.1
787.3	5.8 ± 0.1	4.5	0.008	117	0.20	131	7.1	3.04	0.096	<0.0002	9.0	0.002	0.00293	9.29	2653	9.1
1003.2	5.7 ± 0.1	4.6	0.022	139	0.15	129	7.5	3.19	0.026	<0.0002	8.6	0.001	0.00159	14.13	2633	0.0
1316.0	5.5 ± 0.1	4.5	0.024	135	0.14	130	7.0	3.08	0.017	<0.0002	8.3	0.001	0.00168	17.71	2637	2.1
Quench ^d	6.5 ± 0.1	6.7	0.016	118	0.78	113	6.4	6.52	0.030	0.01	6.8	0.002	0.01147	12.26	–	1.4
Uncertainty ± 1Σ ^j	–	–	0.005	9	0.05	6	0.4	0.09	0.001	–	0.5	0.003	0.00001	±3.0%	–	–
Predicted equilibrium value ^e , pre-injection	–	7.2	–	138	0.62	129	10.0	0.11	2E-05	0.000008	6.3	0.003	–	–	0.1	–
predicted equilibrium value ^e , post-injection	–	5.5	–	138	0.62	157	2.9	0.34	0.006	0.08	6.1	0.002	–	–	2570	–

NI = not included because data appear anomalous.

^a Bench measurements at 20 °C and 0.1 MPa.

^b Calculated, see Section 2.3 for explanation.

^c Unreacted water composition.

^d Water composition after termination of experiment; In situ pH calculated at standard conditions.

^e See Section 2.3 for explanation.

^f Measured values correspond to sample collected for bench pH; See Section 3.4 for additional explanation.

^g (*Italicized*) Pre-injection in situ values assumed to be same as bench values; See Section 3.4 for additional explanation.

^h (**Bold**) Post-injection in situ values calculated; See Sections 2.3 and 3.4 for additional explanation.

ⁱ Charge balance includes minimal phosphate and bromide values, as well as calculated bicarbonate values (not shown).

^j One standard deviation of in-house standard ($n = 8$ for EXP-1, -2, and -3; $n = 7$ for EXP-4 and -5).

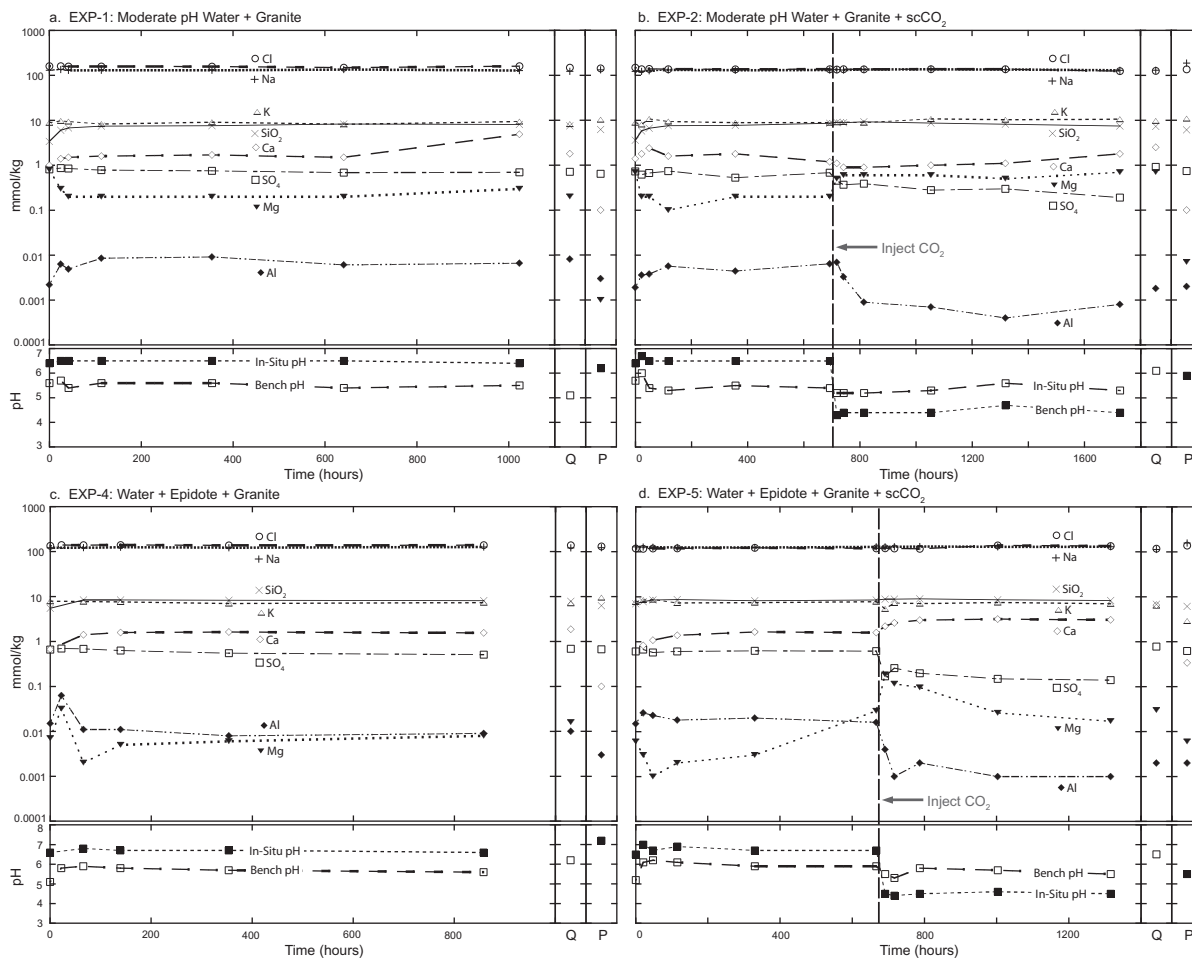


Fig. 1. Water chemistry as a function of time for (a) the water–granite experiment, EXP-1, (b) the moderate pH water–granite– scCO_2 experiment, EXP-2, (c) the water–epidote–granite experiment, EXP-4, and (d) the water–epidote–granite– scCO_2 experiment, EXP-5. Major ion concentrations and pH are plotted for each experiment. On the right of each graph, quench geochemistry (at 25 °C, 0.1 MPa) and predicted equilibrium states are plotted for each experiment in the columns labeled ‘Q’ and ‘P,’ respectively. The initial water composition (25 °C, 0.1 MPa) is plotted along the y-axis in each case.

time. Post-injection concentrations of $\text{SiO}_2(\text{aq})$ gradually decrease over time. Not all analytes establish a steady-state concentration by the end of these experiments, including $\text{SiO}_2(\text{aq})$, Ca, Mg, SO_4 , and Al in EXP-2 and $\text{SiO}_2(\text{aq})$ and Ca in EXP-3.

The water–epidote–granite experiment (EXP-4) and the pre-injection stage of the water–epidote–granite– scCO_2 experiment (EXP-5) display relatively constant concentrations of Cl, Na, K, and SO_4 and increasing concentrations of $\text{SiO}_2(\text{aq})$ and Ca (Fig. 1c and d). Concentrations for these analytes approach steady state at the termination of EXP-4 and prior to injecting scCO_2 into EXP-5. Concentrations for Al and Mg vary more irregularly over time, but also approach a steady-state concentration, with the exception of Mg in EXP-5.

Post-injection concentrations of Cl, Na, and K are relatively constant for EXP-5 (Fig. 1d). Concentrations of $\text{SiO}_2(\text{aq})$ and Ca appear to increase during the first 5 days after scCO_2 injection while SO_4 and Al concentrations decrease over the same period of time. Post-injection concentrations of Mg increase abruptly and then gradually

decrease over time. With the exception of Mg, these analytes appear to establish a steady-state concentration prior to the end of the experiment.

When an experiment is cooled and depressurized, it is important to collect samples to identify dissolution or precipitation reactions that may be artifacts of the termination process. We refer to this process as ‘quenching’ and to the samples as ‘quench’ samples. The quench sample data are included in Table 3 and shown on Fig. 1 in the columns labeled ‘Q’. Quench samples contain higher concentrations of Ca, SO_4 , and Al and lower concentrations of K compared to the samples collected just prior to quenching. In two cases, EXP-1 and -5, concentrations of $\text{SiO}_2(\text{aq})$, Na, and Cl also decrease.

Increased Ca and SO_4 suggest possible dissolution of a calcium sulfate during the quench process; we observed no minerals that could explain this observation. Decreased $\text{SiO}_2(\text{aq})$, Na, Cl, and possibly K suggest potential precipitation of silica and/or halite/sylvite. We observed no salts, but these may have dissolved in the deionized water used to rinse recovered minerals. We did identify examples of

Table 4
Comparison of predicted vs. observed secondary minerals at 250 °C.

Description	EXP-1		EXP-2		EXP-3		EXP-4		EXP-5		Field ^b
	Water + granite		Moderate pH water + granite + scCO ₂		Low pH Water + granite + scCO ₂		Water + epidote + granite		Water + epidote + granite + scCO ₂		
	P	O	P	O	P	O	P	O	P	O	
Illite ^a	X	X	X	X	X	X		X	X	X	X
Smectite	X			X		X		X	X	X	
Zeolite	X	?		?		?		X	X		X
Carbonate			X		X				X		X
Quartz	X		X		X			X		X	X
Albite	X										X
K-feldspar	X							X			X
Epidote								X			X
Prehnite								X			X
Fe-oxide/sulfide	X		X			X					X

P = predicted mineral, O = observed mineral, X = predicted or observed mineral, ? = suspected mineral; positive identification not possible.

^a Proxy minerals such as muscovite and phengite are included in this category.

^b Commonly observed alteration minerals observed in hydrothermal fields at 250 °C (Henley and Ellis, 1983).

silica precipitation in both EXP-1 and -5. Increased concentrations of Al are more difficult to explain, especially with the competing Ca–Na–K–Si reactions already identified.

A compelling observation is the contrast in SiO₂(aq) evolution in the post-injection stages of the water–granite–scCO₂ experiment, EXP-2, and the water–epidote–granite–scCO₂ experiment, EXP-5. In EXP-2, SiO₂(aq) concentrations gradually decrease post-injection whereas in EXP-5, concentrations approach a steady-state. Although we have no way to qualitatively or quantitatively define this relationship, these differences are likely due to the compositions and proportions of smectite and illite that evolved during the later part of each experiment.

3.4. Total dissolved inorganic carbon

Table 3 includes ΣCO₂(aq) ‘bench’ analyses that correspond to degassed and cooled samples exposed to atmosphere. Unreacted water used in the experiments started with approximately 0.1 mmol/kg ΣCO₂(aq), and after exposure to compressed air during reaction cell leak tests, increased to a maximum of 0.8 mmol/kg. We also observe variability in the amounts of ΣCO₂(aq) measured during the water–rock stage of each experiment (0.1–0.8 mmol/kg) and attribute this to reduced instrument precision near the method detection limit. For these samples, contamination (from leak testing with compressed air) and analytical precision pose no problem since ΣCO₂(aq) is significantly undersaturated during the water–rock stage of each experiment and no carbonate minerals are present at the beginning of the experiments.

We exclude results for in situ ΣCO₂(aq) measurements because of difficulties collecting consistent samples of exsolved CO₂ from CO₂-saturated experiments. In order to conduct geochemical modeling (Section 2.3), we use calculated ΣCO₂(aq) concentrations (Table 3). We are able to substitute calculated for measured values because

experiments were saturated with respect to post-injection ΣCO₂ (Section 2.1). An executable file available from Duan and Sun, representing their 2003 equation of state for CO₂, was used for these calculations (Sun, 2011, personal communication).

3.5. pH

pH measurements taken in the presence of atmosphere and at 20 °C and 1 bar are included as ‘bench pH’ values in Table 3 and shown on Fig. 1. Granite experiments, EXP-1, -2, and -3, had initial pH values of 5.6, 5.7, and 3.9, respectively. Epidote–granite experiments, EXP-4 and -5, had initial pH values of 5.1 and 5.2, respectively.

In the case of the water–rock segment of each experiment (i.e., no scCO₂), bench pH values fluctuate by as much as ±1.0 over the first 48 h, and then approach steady-state values of 5.4–5.5 in EXP-1, -2, and -3 and 5.6–5.9 in EXP-4 and -5. After injecting scCO₂ into EXP-2, -3, and -5, bench pH values decrease and approach a steady-state value of 5.3–5.4 in EXP-2 and -3 and 5.5 in EXP-5 within a couple of days.

Calculated, in situ pH values are an average of 1.0 unit higher than bench pH values during the water–rock stage of each experiment. For those experiments also injected with scCO₂ (EXP-2, -3, and -5), post-injection in situ pH values are an average of 1.0 unit lower than bench pH values (Table 3 and Fig. 1).

3.6. Theoretical predictions

As predicted by equilibrium calculations, concentrations for Cl, Na, K, and generally SiO₂(aq) (Table 3 and Fig. 1) correspond well to those measured in the last sample before the quench. However, predictions consistently underestimate Ca and Mg concentrations (all experiments), and overestimate SO₄ in experiments with scCO₂ (EXP-2, -3,

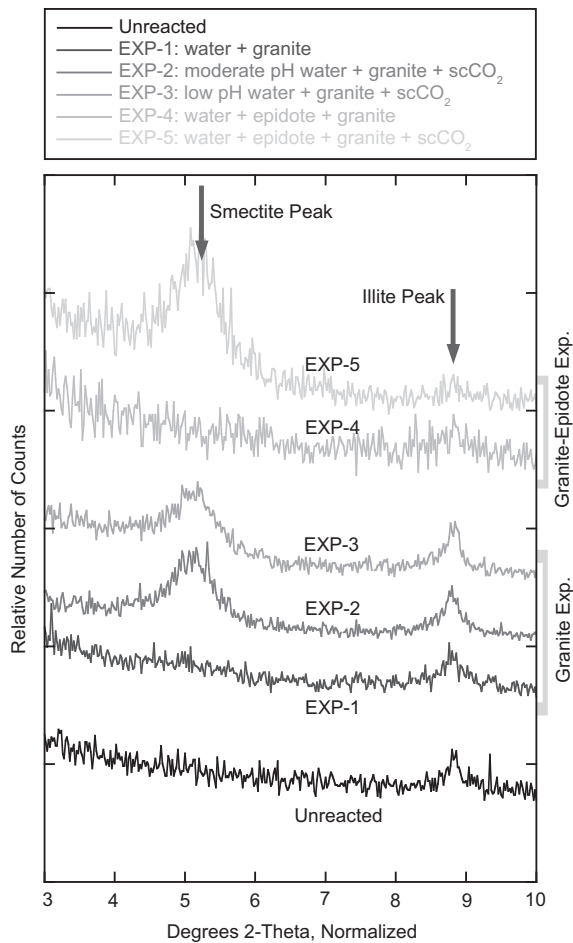


Fig. 2. Normalized and relative XRD diffraction patterns for glycolated clay-fraction samples from the unreacted granite and from each experiment. Noted peaks include illite peaks on right and smectite peaks on left. Illite peaks are evident in samples from the unreacted granite and from water–granite \pm scCO_2 experiments (EXP-1, -2, and -3). Illite peaks are less defined in the water–epidote–granite \pm scCO_2 experiments (EXP-4 and -5). Smectite peaks are only evident in experiments with CO_2 , including water–granite– CO_2 experiments (EXP-2 and -3) and the water–epidote–granite– CO_2 experiment (EXP-5).

and -5). Predicted aluminum concentrations are an average of $\sim 53\%$ higher than measured concentrations in EXP-2, 3, and -5 and an average of $\sim 61\%$ lower in EXP-1 and -4. In addition, the predicted $\text{SiO}_2(\text{aq})$ concentration is $\sim 26\%$ lower than measured in EXP-5.

Calculated and predicted in situ pH values are included in Table 3 and shown on Fig. 1. Predicted in situ pH is 0.2–0.3 units higher than calculated values in the water–rock stage of the granite experiments (EXP-1, -2, and -3) and 0.5–0.6 units higher in the water–rock stage of the epidote–granite experiments (EXP-4 and -5). Post-injection, in situ pH predictions are 1.1–1.4 units lower than calculated for the water–granite– scCO_2 experiments (EXP-2 and -3) and 1.0 unit lower in the water–epidote–granite– scCO_2 experiment (EXP-5). A comparison of predicted and observed secondary mineralogy is presented in Table 4 and discussed further in Section 4.1.

4. DISCUSSION

4.1. Experimental vs. theoretical results: paths to equilibrium

Here, we compare experimental results with equilibrium predictions to determine the extent of system equilibration, the sequence of water–rock reactions, and the water–rock response to scCO_2 injection. As noted in Section 3.3 and shown in Fig. 1, some major element concentrations reach a steady state over the course of each experiment. Congruence between steady state concentrations and equilibrium predictions (Section 3.6) indicates local equilibrium. In contrast, some major elements do not reach steady state concentrations, which suggests on-going reaction. This observation is consistent with the minerals recovered from the experiment (Table 4); both reactants and products of hydrothermal alteration reactions were recovered (i.e., feldspars as well as clays and zeolites), thus the reactions did not proceed to completion and the experiments did not attain equilibrium. We provide two sets of activity diagrams (Figs. 5 and 6) to clarify reaction progress. Each figure plots data from two experiments, the water–granite– scCO_2 experiment, EXP-2, and the water–epidote–granite– scCO_2 experiment, EXP-5. The other experiments display similar relationships as those shown in Figs. 5 and 6.

Fig. 5a and b shows mineral stability fields, aqueous species activities for each sample, and the final predicted equilibrium state in the $\text{CaO–Al}_2\text{O}_3\text{–SiO}_2\text{–H}_2\text{O–CO}_2$ system for EXP-2 and -5, respectively. Two diagrams are shown for each experiment and include stability fields for experimental conditions just prior to scCO_2 injection (on left) and after scCO_2 injection and just prior to quenching (on right). Notice the calcite stability field increases significantly with addition of scCO_2 (see figure caption for other conventions). Fig. 6a and b similarly show mineral stability relationships, aqueous species activities, and the final predicted equilibrium state for the $\text{K}_2\text{O–Al}_2\text{O}_3\text{–SiO}_2\text{–H}_2\text{O–CO}_2$ system. In Fig. 6, the stability fields do not shift with addition of scCO_2 , so pre- and post-injection data are shown on one plot for each experiment. We use heulandite, clinoptilolite-Ca, and mordenite-K as proxy minerals for higher temperature hydrothermal zeolites (i.e., wairakite); beidellite-Ca and beidellite-K serve as proxy minerals for hydrothermal smectites; and muscovite serves as a proxy mineral for illite. The broader mineral group names are used in the following discussion.

The reaction paths in all of the diagrams approach or track along the chalcedony stability boundary, indicating saturation with chalcedony and supersaturation with quartz. This trend is best explained by the Ostwald step rule (e.g., Rimstidt and Barnes, 1980; Stumm and Morgan, 1996). Applying this rule to our system (or a natural system), it is not unreasonable to find that silica activity is initially controlled by chalcedony instead of quartz; the Ostwald step rule permits chalcedony precipitation prior to quartz because chalcedony has a higher solubility and lower fluid–rock interfacial tension than quartz. As previously noted, we observe no silica that formed at in situ experimental conditions, but based on this discussion, if we had, it is likely that it would have been chalcedony.

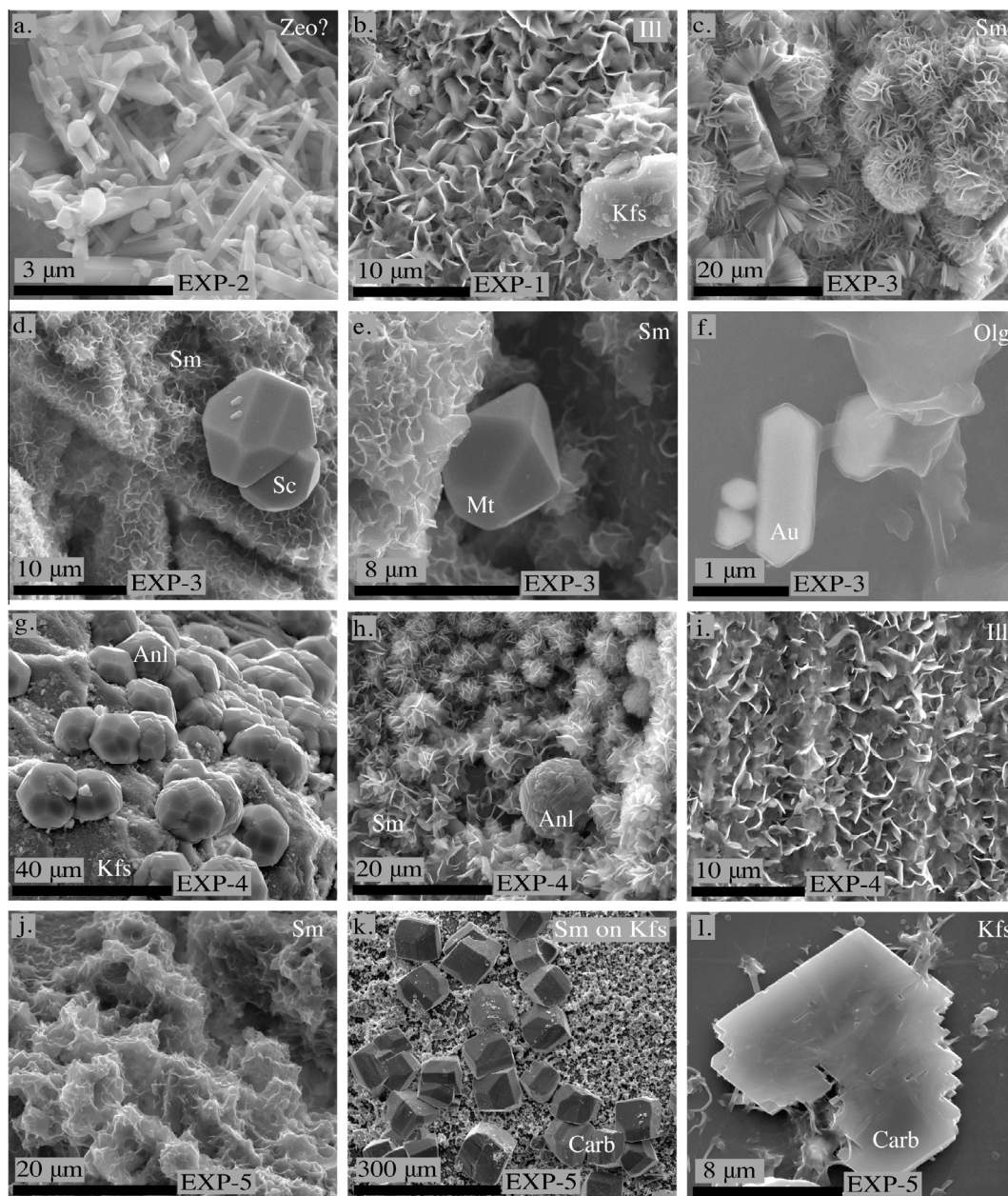


Fig. 3. FE-SEM micrographs of secondary minerals. Each image includes a scale as well as labels for the mineral(s) and associated experiment. Images (a) and (b) show typical needle-forming aluminosilicate (zeolite?) and illite petals, respectively, as observed in granite experiments, EXP-1, -2, and -3. (c) Typical rosette-forming smectite, as observed in scCO_2 -containing granite experiments, EXP-2 and -3. Morphology is consistent with euhedral growth in open space. Images (d)–(f) show scheelite, magnetite, and gold, as observed in the low pH water–granite– scCO_2 experiment, EXP-3. (g) Analcime, as observed in the water–epidote–granite experiment, EXP-4. (h) Analcime in a bed of rosette-forming smectite, as observed in EXP-4. (i) Illite, as observed in EXP-4. (j) Poorly-formed smectite, as observed in scCO_2 -containing water–epidote–granite experiment, EXP-5. Images (k) and (l) show blocky and rhombohedral Ca-carbonates from EXP-5. Mineral abbreviations: analcime = Anl; carbonate = Carb; gold = Au; illite = Ill; K-feldspar = Kfs; magnetite = Mt; oligoclase = Olg; scheelite = Sc; smectite = Sm; and zeolite = Zeo.

We also note that calculations for the final predicted equilibrium state allowed quartz precipitation (Section 2.3), so predictions necessarily lie along the quartz stability boundary and include quartz (Table 4, Section 3.6). This has introduced a bias towards lower silica activities for the final predicted equilibrium state. If calculations allowed chalcedony precipitation, then the predicted equilibrium

states would align with the chalcedony boundary, and therefore, more closely match observed results. In our assessment of reaction path progress for each activity diagram below, we ignore this bias.

In the water–granite– scCO_2 (EXP-2) diagram, species activities for pre-injection samples define a reaction path that moves from prehnite to zeolite stability (Fig. 5a) and

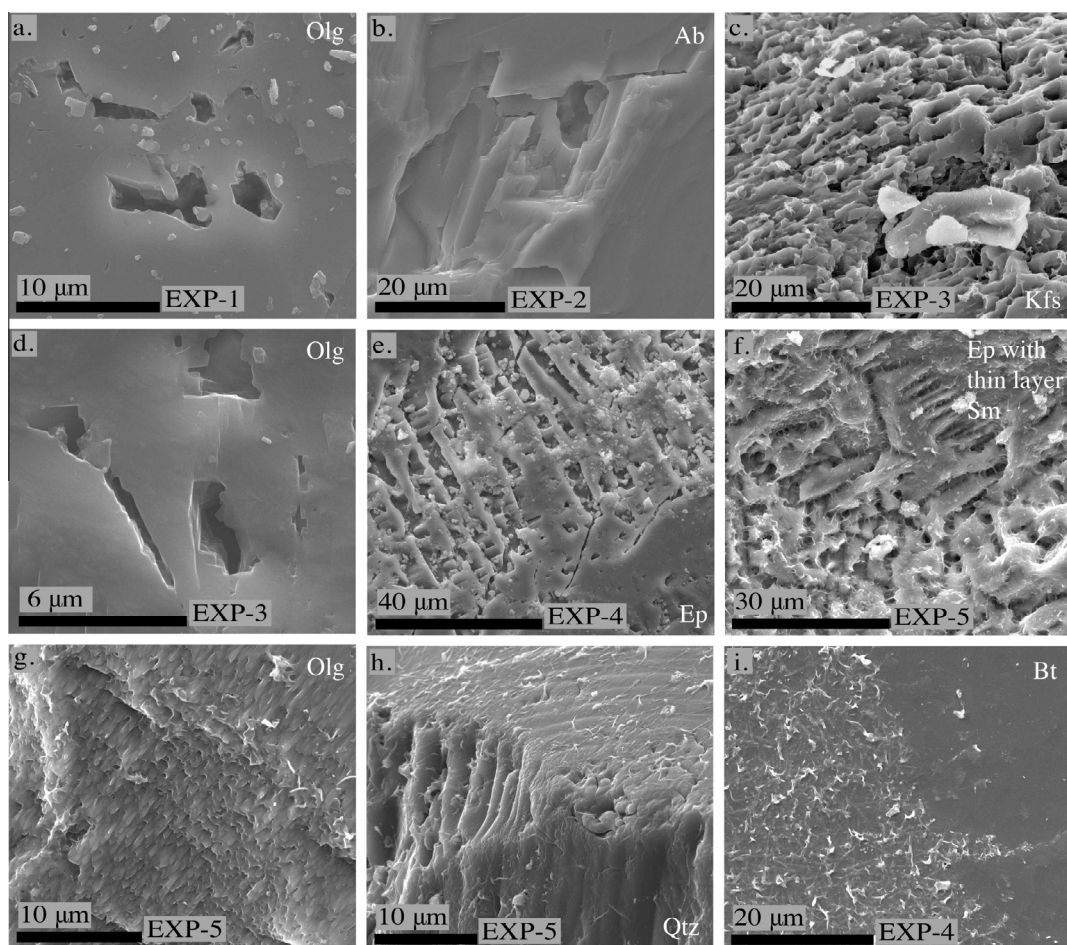


Fig. 4. FE-SEM micrographs of mineral dissolution textures. Each image includes a scale as well as labels for the mineral(s) and associated experiment. Images (a)–(d) represent typical dissolution pitting/etching in oligoclase, albite, and K-feldspar in the granite experiments (EXP-1, -2, and -3). Progressively more dissolution is evident in feldspars from scCO_2 -injected experiments (EXP-2 and -3). Images (e) and (f) respectively show epidote dissolution in the water–epidote–granite experiment (EXP-4) and the water–epidote–granite– scCO_2 (EXP-5). As seen in (f), some epidote surfaces in EXP-5 are coated with a thin layer of smectite. Images (g) and (h) respectively show oligoclase and quartz dissolution in EXP-5. As shown in image (i), biotite does not exhibit dissolution textures, but clay minerals precipitate on biotite surfaces in all experiments. Small nodules present in images (a), (c), (f) and elsewhere are primary mineral powders and not secondary mineral products. Mineral abbreviations: albite = Ab; biotite = Bt; epidote = Ep; K-feldspar = Kfs; oligoclase = Olg; quartz = Qtz; and smectite = Sm.

from microcline to zeolite stability (Fig. 6a) The reaction paths terminate near the predicted equilibrium state within the zeolite stability field (Fig. 5a) or on the zeolite–illite stability boundary (Fig. 6a). These predicted minerals correspond to minerals precipitated in the experiments (Table 4). Our observations indicate the pre-injection stage of EXP-2 closely approached equilibrium.

The post-injection reaction path for EXP-2 abruptly swings into the smectite stability field (Figs. 5a and 6a), then moves towards the predicted equilibrium state within the carbonate stability field (Fig. 5a) and along the illite–microcline stability boundary (Fig. 6a). The reaction path falls just short of achieving the predicted equilibrium state. Given additional time, the experiment may have achieved equilibrium. The stable minerals predicted by the position of the final aqueous activities, smectite (Fig. 5a) and illite (Fig. 6a), correspond to minerals observed in the post-injection stage of EXP-2 (Table 4). In addition, the terminus of

the reaction path in Fig. 5a agrees with the absence of carbonate in this experiment.

With respect to the water–epidote–granite– scCO_2 (EXP-5) diagrams, species activities for pre-injection samples cluster in the zeolite, smectite (Fig. 5b), and illite (Fig. 6b) stability fields. The reaction paths terminate far from the predicted equilibrium state, indicating the system did not approach equilibrium prior to injecting scCO_2 . The minerals predicted by the terminus of the reaction path correspond to minerals that precipitated in the experiments, including illite and zeolite (Table 4).

The post-injection reaction path for EXP-5 also shows an abrupt swing into the smectite stability field. The reaction path then moves towards the predicted equilibrium state along the carbonate–smectite stability boundary (Fig. 5b) and within the illite stability field (Fig. 6b). As with results for EXP-2, the reaction paths do not achieve the predicted equilibrium state. Predictions for secondary

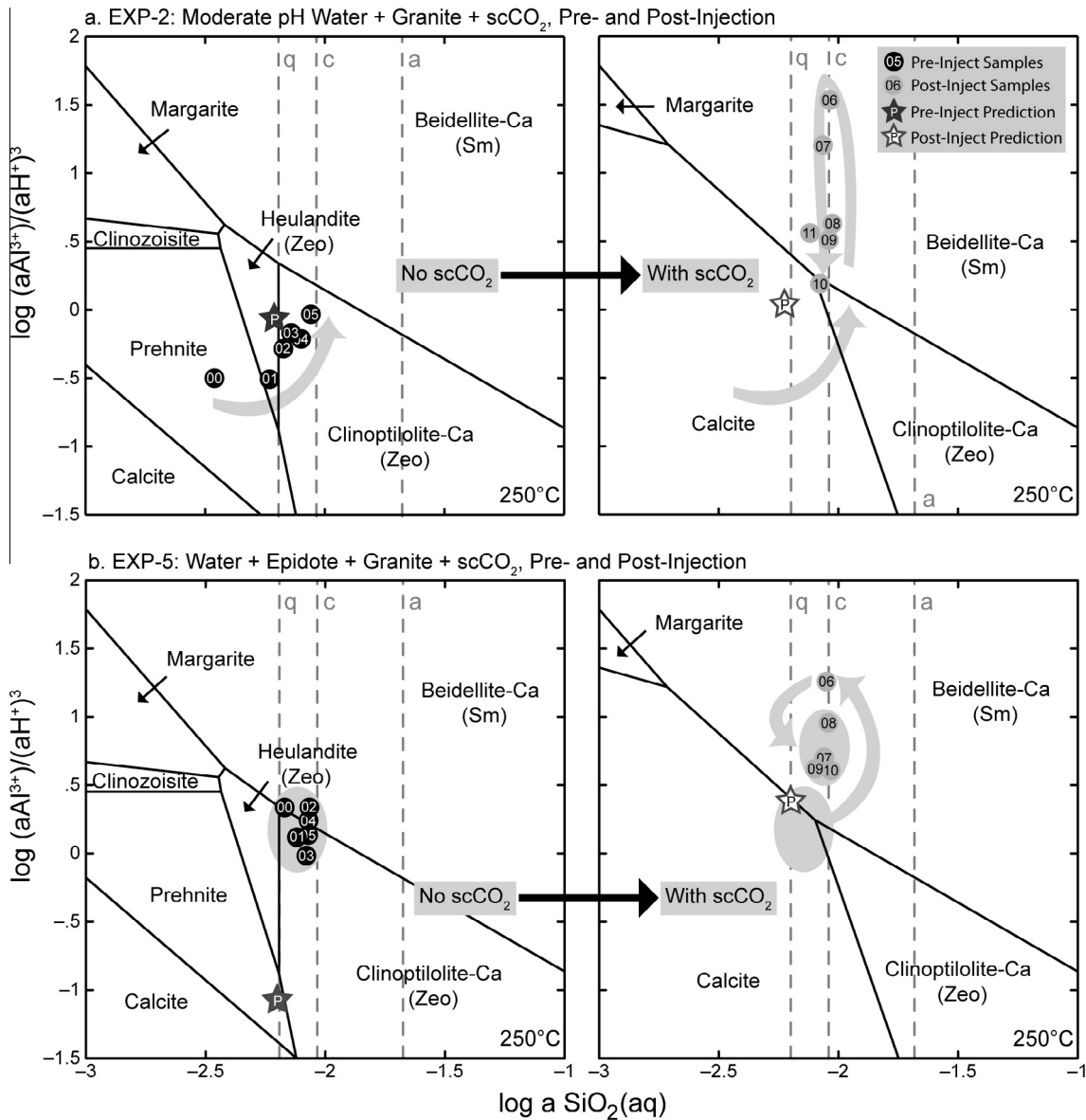


Fig. 5. Mineral stability relationships, aqueous species activities for individual samples, and predicted equilibrium states in the CaO–Al₂O₃–SiO₂–H₂O–CO₂ system for (a) the water–granite–scCO₂ experiment, EXP-2 and (b) the water–epidote–granite–scCO₂ experiment, EXP-5. Two diagrams are shown for each experiment and include stability fields for experimental conditions immediately prior to scCO₂ injection (on left) and after scCO₂ injection and immediately prior to terminating the experiment (on right). The dashed, vertical lines represent saturation with respect to quartz ('q'), chalcedony ('c'), and amorphous silica ('a'). Activities for aqueous species in sequential, pre-injection samples are on the left side; activities for aqueous species in post-injection samples are on the right side. Wide, gray arrows indicate the general path to equilibrium within each experiment. Predicted pre- and post-injection equilibrium states are shown using dark and light-colored stars, respectively. Mineral abbreviations: smectite = Sm and zeolite = Zeo.

minerals agree with the presence of illite and smectite in EXP-5 (Table 4). In addition, the terminus of the reaction path in Fig. 5b agrees with the absence of carbonate in this experiment.

The changes in reaction paths in response to scCO₂ injection merit comment. Initially, the abrupt increase in $\log(a\text{Al}^{3+})/(a\text{H}^+)^3$ drives the reaction pathways away from predicted equilibrium activities with calcite (Fig. 5) and illite (Fig. 6). Activities for H⁺ and Al³⁺ of individual

samples (collected just prior to and just after scCO₂ injection) increase by 2 and 8 orders of magnitude, respectively. The Al³⁺ activity initially exceeds H⁺ activity. Over time, Al³⁺ activity gradually decreases driving the reaction pathways back towards predicted equilibrium.

The activity diagrams for the low pH water–granite–scCO₂ experiment (not shown for brevity), EXP-3, are similar to those shown for EXP-2 (Figs. 5 and 6) with one significant difference: $\log(a\text{Al}^{3+})/(a\text{H}^+)^3$ of some of

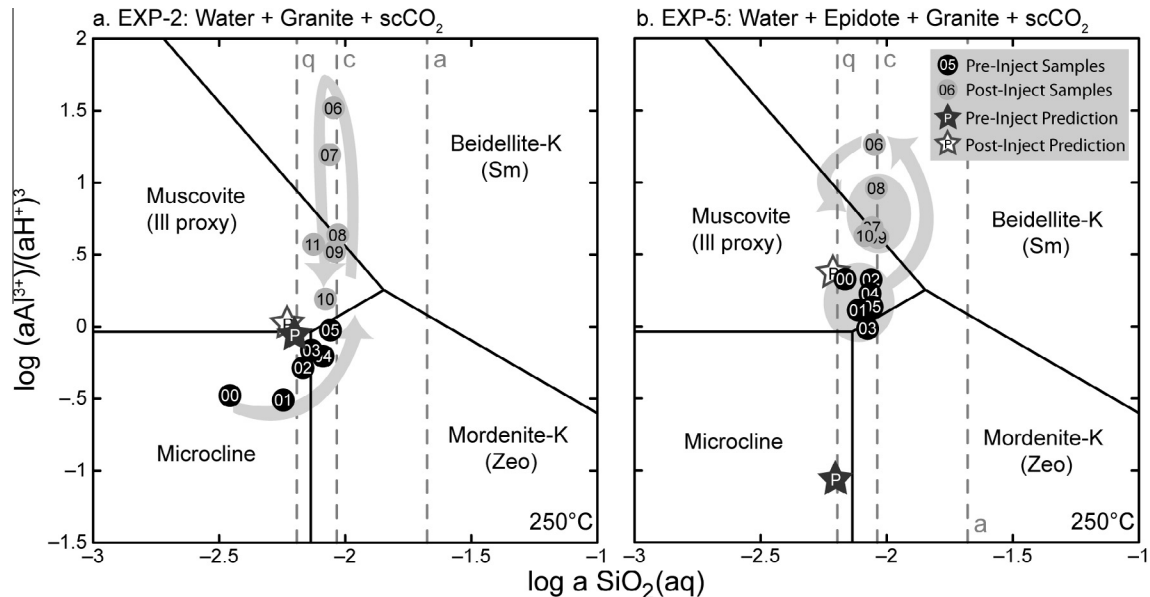


Fig. 6. Mineral stability relationships, aqueous activities for individual samples, and predicted equilibrium states in the $K_2O-Al_2O_3-SiO_2-H_2O-CO_2$ system for (a) the water–granite– $scCO_2$ experiment, EXP-2 and (b) the water–epidote–granite– $scCO_2$ experiment, EXP-5. Pre- and post-injection stability fields do not shift with addition of $scCO_2$, so there is only one diagram for each experiment. The dashed, vertical lines represent saturation with respect to quartz ('q'), chalcedony ('c'), and amorphous silica ('a'). Activities for aqueous species in sequential, pre-injection samples are shown with dark-colored circles; activities for aqueous species in post-injection samples are shown with light-colored circles. Wide, gray arrows indicate the general path to equilibrium within each experiment. Predicted pre- and post-injection equilibrium states are shown using dark and light-colored stars, respectively. Mineral abbreviations: illite = Ill; smectite = Sm; and zeolite = Zeo.

the initial samples are an order of magnitude lower than those for the moderate pH experiment, EXP-2. This difference reflects the initial abundance of hydrogen ions in EXP-3 and is noteworthy because, with continued reaction, the system achieves similar pH and aqueous species concentrations as EXP-2. This observation highlights the buffering capacity of granite on fluid compositions (See also Section 4.2.2).

4.2. Results in the context of natural systems

4.2.1. Comparison of secondary mineralogy

In Fig. 7 we show: (1) the secondary mineralogy developed in our experiments; (2) the generalized secondary

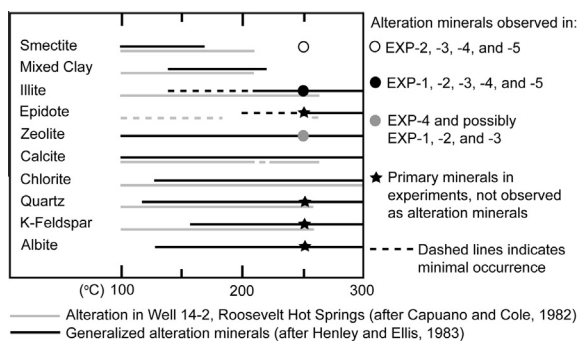


Fig. 7. A comparison among secondary mineralogy in experiments, generalized secondary mineralogy found in natural systems, and secondary mineralogy from a deep-seated well in the Roosevelt Hot Springs Geothermal Field.

mineralogy found in hydrothermal systems developed in silicic rocks between 100 and 300 °C (Henley and Ellis, 1983); and (3) the secondary mineralogy from a deep-seated well in the Roosevelt Hot Springs Geothermal Field (Capuano and Cole, 1982). Fig. 7 indicates the presence of illite and zeolite in many natural systems at 250 °C. For example, illite exists in the Roosevelt Hot Springs field, and illite and zeolite both exist in the silicic rocks of Ohaaki-Broadlands, New Zealand (Browne and Ellis, 1970) and Wairakei, New Zealand (Steiner, 1968). These field observations corroborate illite formation in our experiments. Corroboration of zeolite is more tenuous since the analcime and other possible zeolites that precipitated are lower-temperature varieties than those expected at 250 °C.

Mixed-layer clays, epidote, calcite, chlorite, quartz, K-feldspar, and albite commonly occur as secondary minerals in natural systems, but these minerals were not observed in the experiments as secondary minerals (Fig. 7). This is not unexpected as many parameters affect mineral stability in hydrothermal systems, including temperature, host rock composition, permeability, fluid composition, reaction time, water:rock ratio, boiling, mixing, and conductive cooling (e.g., Browne, 1978; Ellis, 1979; Rose and Burt, 1979; Henley and Ellis, 1983). For example, calcite is common in CO_2 -rich systems such as Ohaaki-Broadlands (Browne and Ellis, 1970), whereas epidote and wairakite are more commonly observed in CO_2 -poor systems such as Wairakei (Steiner, 1968). These field observations are consistent with our predicted results for carbonate stability in the CO_2 -rich experiments (EXP-2, -3, and -5) (Figs. 5 and 6) as well as the predicted and observed dissolution of

epidote in the water–epidote–granite–CO₂ experiment, EXP-5 (Fig. 4f).

Silica stability in natural systems also informs us about our experimental results. Natural geothermal waters above 180 °C are often in equilibrium with quartz (Fournier and Rowe, 1966; Mahon, 1966; Fournier, 1983). Our calculations also indicate quartz should control silica saturation in the experiments. However, we do not observe secondary quartz attributable to formation at 250 °C even though our calculations suggest oversaturation with quartz. This discrepancy confirms that our experiments did not achieve equilibrium. Additionally, natural geothermal fluids are often quartz-saturated at depth and, upon ascent, SiO₂(aq) concentrations increase. Resulting fluids precipitate amorphous silica or opal at or near the surface (Fournier and Rowe, 1966; Rimstidt, 1997). Quench-related silica observed in EXP-1 and -5 (Sections 3.1 and 3.3) forms by the analogous process of cooling and depressurizing the completed experiment.

The most conspicuous difference among our results, other published experimental results (Appendix A), and natural systems (Fig. 7) is that smectite is commonly produced in experiments at temperatures up to 500 °C but is unstable in natural systems at temperatures above 180–220 °C (Henley and Ellis, 1983). Our most reliable understanding of smectite stability comes from natural systems (e.g., Reyes and Cardile, 1989; Schiffman and Fridleifsson, 1991; Inoue et al., 1992; Beaufort et al., 1995; Patrier et al., 1996; Fulignati et al., 1997; Gianelli et al., 1998; Rigault et al., 2010), so it follows that we rely on the geochemistry and mineralogy of these systems to help us interpret smectite ‘stability’ and the drivers of smectite formation at temperatures greater than 220 °C. Since stable smectite is not observed in natural systems at 250 °C, our geochemical predictions of stable smectite are probably inaccurate. We attribute this inaccuracy to poorly constrained thermodynamic data for systems containing complex, solid-solution minerals such as smectite, illite, and zeolite (e.g., Langmuir, 1997).

In comparing our results to natural systems, we also infer that smectite in our experiments is metastable. High temperature smectites are recognized as metastable in natural systems, with formation generally in response to physico-chemical processes including mixing and/or boiling (e.g., Beaufort et al., 1995; Patrier et al., 1996; Fulignati et al., 1997; Rigault et al., 2010). Smectite in high temperature regimes has also been explained as a relict phase (e.g., Schiffman and Fridleifsson, 1991; Rigault et al., 2010) that may persist due to kinetics and/or shielding caused by swelling clays that prevent continued fluid–rock interaction (Reed, 1997).

In addition to temperature changes, there are a variety of factors that can account for variations in clay formation among theoretical, experimental, and natural systems including water:rock ratio (e.g., Seyfried and Bischoff, 1977; Giggenbach, 1984; Savage et al., 1987; Whitney, 1990), permeability (e.g., Patrier et al., 1996; Fulignati et al., 1997), silica activity or stability (e.g., Giggenbach, 1988; Abercrombie et al., 1994; Hutcheon et al., 1994; Vidal et al., 2012), kinetics (e.g., Mottl and Holland,

1978; Schiffman and Fridleifsson, 1991; Patrier et al., 1996), CO₂ concentrations (e.g., Giggenbach, 1984), and/or iron and magnesium content (e.g., Mottl and Holland, 1978; Reyes and Cardile, 1989). We believe metastable smectite formed in our experiments due to a combination of factors including kinetics and relatively high (1) water:rock ratios; (2) silica activities; (3) CO₂ concentrations; and (4) magnesium–iron concentrations (Section 3.1).

4.2.2. Application of results to other natural systems

Our results also apply to other natural processes such as the buffering capacity of granitic rocks, styles of clay formation, and tungsten ore formation. During pluton emplacement and cooling, magmatic volatiles such as CO₂, SO₂, HCl, and H₂O escape outwards and mix with local meteoric groundwater. As warm, acidic fluids ascend, they react with country rock and become progressively neutralized because of the buffering capacity of the wall rock. This progression has implications for the evolution of ore fluids and is commonly observed in epithermal and porphyry copper deposits (e.g., Reed, 1997 and references therein). Our experimental work simulates this type of process, although at higher pH. The pre-injection stage of the low pH water–granite–scCO₂ experiment, EXP-3, shows how HCl-rich fluids might interact with wall rock. Over a period of 28 days, the pH of this experiment increases from 3.9 to 6.5 (Table 3) demonstrating the capacity of the granite to buffer acidic fluids. This buffering capacity is consistent with neutral pH conditions and processes in many natural geothermal systems (Ellis, 1979; Reed, 1997).

The morphology of clay minerals (illite and smectite) formed in our experiments also elucidates specific processes in natural systems. In particular, hydrothermal clay formation is thought by some to mimic that of diagenetic clay formation whereby smectite is a precursor to illite, with the conversion taking place due to increasing temperature (e.g., Inoue et al., 1992). Other researchers suggest hydrothermal clay formation can proceed via direct precipitation (e.g., Bethke et al., 1986; Wang and Xu, 2006). This debate also ties into field observations that document the formation of smectite and mixed-layer illite/smectite at temperatures (<~220 °C) lower than those required for the formation of illite (Henley and Ellis, 1983; Inoue, 1995). Illite and smectite may be present in hydrothermal rocks as distinct minerals or as mixed-layer illite/smectite (Inoue, 1995). In our experiments, illite and smectite exhibit no textural evidence for interlayering or prograde reactions. Smectite precipitation occurred only after scCO₂ injection, and its morphology is suggestive of precipitation in open spaces (Fig. 3c). In the context of the debate regarding hydrothermal clay formation, therefore, our experimental results indicate that: (1) temperature may not always dictate clay formation (see also Section 4.2.1); and (2) clays can precipitate directly from solution.

Scheelite precipitated in the low pH water–granite–scCO₂ experiment (EXP-3) but not in any of the other experiments. Although tungsten was introduced as a contaminant (Section 3.1), it is appropriate to explore mechanisms for scheelite formation since it is found naturally in granitic hydrothermal systems (Hedenquist and

Lowenstern, 1994). Homogenization temperatures of fluid inclusions in scheelite range from 200 to 400 °C, with most occurrences ranging from 200 to 300 °C (Naumov et al., 2011). Fluid inclusion data also suggest that scheelite is more prevalent in association with CO₂-rich fluids (Naumov et al., 2011). Formation of scheelite in EXP-3, therefore, corroborates available fluid inclusion data for natural systems.

4.3. Implications for engineered systems

Our results have implications for conventional geothermal systems (including CPG), non-conventional geothermal systems (including EGS), and CCS reservoirs with respect to porosity/permeability changes, geothermal capping or cap thickening, and carbon sequestration potential. Upon initial development of a system, with or without scCO₂, the most obvious impacts may be on porosity and permeability. Our experiments indicate water–rock systems without scCO₂ precipitate illite and that water–rock–scCO₂ systems precipitate smectite. This generalization applies to both water–granite ± scCO₂ and water–epidote–granite ± scCO₂ systems. Therefore, with respect to water-based and CO₂-based geothermal operations, operators may anticipate illite and smectite precipitation, respectively, within production pathways. Illite and especially smectite, a swelling clay, have the potential to greatly affect reservoir porosity and permeability. For example, sandstones with even a few percent smectite will, in general, exhibit orders of magnitude lower permeability than sandstones of the same porosity but no clay content (Nelson, 1994; McPherson and Bredehoeft, 2001). Clays may similarly form in and affect deep, arkosic reservoirs targeted for carbon sequestration projects. With continued reaction time, carbonate and/or silica precipitation may also affect the porosity/permeability of exploited granitic or arkosic reservoirs.

Our results also indicate the possibility of either creating or thickening a geothermal cap due to mineral precipitation within or on the edges of a targeted reservoir. In nature, geothermal caps reduce permeability above the main heat-producing reservoir and generally form as a result of silica and silicate deposition triggered by boiling, mixing of warm CO₂-charged, NaCl–waters and cold meteoric waters, or interaction of steam and gas with cold meteoric waters (Mahon et al., 1980; Hedenquist, 1990; Simmons and Browne, 2000). In this study, experiments emulate conditions under which geothermal caps form in natural systems: NaCl–waters used in the pre-injection experimental segments are ‘mixed’ with CO₂, after injection, causing precipitation reactions that mimic creation or thickening of a geothermal cap. Disadvantages and benefits of such a geothermal cap should be considered during development and utilization of geothermal systems.

Our experimental results also contribute to research addressing possible carbon sequestration in granite-hosted reservoirs (e.g., Liu et al., 2003; Ueda et al., 2005; Suto et al., 2007; Lin et al., 2008) and arkosic reservoirs (e.g., Kaszuba et al., 2005; Rosenbauer et al., 2005; Mandalaparty et al., 2011). With respect to mineral

trapping, where carbon is sequestered by carbonate minerals, our models predict carbonate formation after injection of scCO₂ into the experiments. However, carbonates did not precipitate until the experiments were terminated (i.e., cooled and degassed). Cooling and degassing of scCO₂-bearing fluids in geothermal reservoirs may likewise lead to carbonate mineralization and plugging of near-surface production pathways. By analogy to our experiments, carbonate mineralization in geothermal reservoirs containing scCO₂-bearing working fluids is not expected until later in production. With respect to dissolution trapping, whereby carbon is stored in the water, carbonic acid concentrations increase significantly after injection of CO₂ into experiments (EXP-2, -3, and -5). Thus, dissolution trapping may be a viable sequestration mechanism early in a geothermal operation.

5. CONCLUSIONS

This paper describes experimental results and geochemical models in systems containing water + granite ± epidote ± scCO₂ at temperatures typical of hot geothermal reservoirs (250 °C). Results and implications follow.

- (1) At high water:rock ratios (20:1–10:1), feldspar and epidote are the most reactive minerals. Secondary minerals include illite ± smectite ± zeolite(?), and waters are supersaturated with respect to quartz and saturated with respect to chalcedony.
- (2) Mineral stability relationships, aqueous geochemistry, and experimental observations are self-consistent and suggest that fluid–rock interactions do not achieve the predicted equilibrium states at laboratory time scales.
- (3) Smectite, not carbonate, precipitates in experiments after injection of scCO₂.
- (4) Smectite is predicted as a stable mineral in the water–epidote–granite ± scCO₂ experiments (EXP-4 and -5). However, these predictions are demonstrated to be inaccurate due to incomplete thermodynamic data. In the context of other available research, we believe smectite is metastable in all of our experiments and has formed due to kinetics and relatively high water:rock ratios, silica activities, CO₂ concentrations, and magnesium–iron concentrations.
- (5) Experimental results corroborate natural processes relating to the buffering capacity of granites, the drivers of clay formation, and tungsten ore formation.
- (6) Metastable clay precipitation is likely in granite- or arkosic-hosted engineered systems. Illite may be the dominant clay in water-dominated operations, whereas smectite may be the dominant clay in CO₂-based operations. Related porosity and permeability changes need to be understood and addressed to optimize geothermal resource management and sustainability since even very small amounts of clay can affect rock permeability by orders of magnitude.
- (7) Silicate formation, including clay formation, may create or thicken caps within or on the edges of surrounding engineered reservoirs. Such changes should

be taken into consideration during development, operation, and closure of these systems. In the case of closure, silicate formation may actually help to isolate the system.

- (8) As desired for carbon sequestration projects that coincide with engineered systems, carbonate formation may require extended periods of time, barring degassing of a system. Although mineral trapping mechanisms may be slow, dissolution trapping of carbon species is fast (days), and is a possible mechanism for sequestration in these systems.

Additional experiments evaluating water + granite \pm scCO₂ \pm chlorite \pm calcite interactions have been completed; these experiments are the foundation of our next paper on the subject. Geochemical modeling, including kinetic analysis, is also being conducted on the entire ensemble of experiments (Pan et al., 2012).

ACKNOWLEDGEMENTS

This project is supported by DOE grant DE – EE0002766 to McPherson, Moore, and Kaszuba, the University of Wyoming (UW) School of Energy Resources (SER), and an Encana Corporation graduate assistantship to Lo Ré. The experimental hydrothermal laboratory was constructed with funding from SER. Caroline Lo Ré thanks Virginia Marcon and Mary Kate McCarney (UW) for immeasurable support in the laboratory. We also thank Norbert Swoboda-Colberg and Susan Swapp for XRD and SEM support as well as Kellie Antrobus for BET analyses (UW). We acknowledge Peter Lichtner (Los Alamos National Laboratory) for geochemical modeling assistance and Fred Luiszer (University of Colorado, Laboratory for Environmental and Geological Studies) for aqueous analyses. Three anonymous reviewers and the editor also helped to greatly improve the final manuscript.

APPENDIX A. SUPPLEMENTARY DATA

Supplementary data associated with this article can be found, in the online version, at <http://dx.doi.org/10.1016/j.gca.2014.06.015>.

REFERENCES

- Abercrombie H. J., Hutcheon I. E., Bloch J. D. and de Caritat P. (1994) Silica activity and the smectite–illite reaction. *Geology* **22**, 539–542.
- Beaufort D., Papapanagiotou P., Fujimoto K., Patrier P. and Kasai K. (1995) High temperature smectites in active geothermal systems. In *Water–Rock Interaction* (eds. Y. K. Kharaka and O. V. Chudakov). A.A. Balkema, Rotterdam, Netherlands, pp. 493–496.
- Benson S. and Cook P. (2005) Underground geological storage. In *IPCC Special Report on Carbon Dioxide Capture and Storage. Intergovernmental Panel on Climate Change, Interlaken, Switzerland*. pp. 5.1–5.134 (Chapter 5).
- Bethke C. M. and Yeakel S. (2009) The Geochemist’s Workbench Release 8.0: Reaction Modeling Guide. University of Illinois, Champaign, Illinois.
- Bethke C. M., Vergo N. and Altaner S. P. (1986) Pathways of smectite illitization. *Clays Clay Min.* **34**, 125–135.
- Brown D. (2000) A Hot Dry Rock geothermal energy concept utilizing supercritical CO₂ instead of water. In *Proceedings of the Twenty-Fifth Workshop on Geothermal Reservoir Engineering*. Stanford University, Palo Alto, CA, pp. 233–238.
- Browne P. R. L. (1978) Hydrothermal alteration in active geothermal fields. *Annu. Rev. Earth Planet. Sci.* **6**, 229–250.
- Browne P. R. L. and Ellis A. J. (1970) The Ohaki-Broadlands Hydrothermal Area, New Zealand: mineralogy and related geochemistry. *Am. J. Sci.* **269**, 97–131.
- Brunauer S., Emmett P. H. and Teller E. (1938) Adsorption of gases in multimolecular layers. *J. Am. Chem. Soc.* **60**, 309–319.
- Capuano R. M. and Cole D. R. (1982) Fluid–mineral equilibria in a hydrothermal system, Roosevelt Hot Springs, Utah. *Geochim. Cosmochim. Acta* **46**, 1353–1364.
- Duan Z. H. and Sun R. (2003) An improved model calculation CO₂ solubility in pure water and aqueous NaCl solutions from 273 to 533 K and from 0 to 2000 bar. *Chem. Geol.* **193**, 257–271.
- Duan Z. H., Sun R., Zhu C. and Chou I. (2006) An improved model for the calculation of CO₂ solubility in aqueous solutions containing Na⁺, K⁺, Ca²⁺, Mg²⁺, Cl⁻, and SO₄²⁻. *Mar. Chem.* **98**, 131–139.
- Ellis A. J. (1979) Explored geothermal systems. In *Geochemistry of Hydrothermal Ore Deposits* (ed. H. L. Barnes). John Wiley & Sons, New York, pp. 632–684.
- Fournier R. O. (1983) A method of calculating quartz solubilities in aqueous sodium chloride solutions. *Geochim. Cosmochim. Acta* **47**, 579–586.
- Fournier R. O. and Rowe J. J. (1966) Estimation of underground temperatures from the silica content of water from hot springs and wet-steam wells. *Am. J. Sci.* **264**, 685–697.
- Fulginiti P., Malfitano G. and Sbrana A. (1997) The Pantelleria caldera geothermal system: data from the hydrothermal minerals. *J. Volcanol. Geotherm. Res.* **75**, 251–270.
- Gianelli G., Mekuria N., Battaglia S., Chersicla A., Garofalo P., Ruggieri G., Manganelli M. and Gebregziabher Z. (1998) Water–rock interaction and hydrothermal mineral equilibria in the Tendaho geothermal system. *J. Volcanol. Geotherm. Res.* **86**, 253–276.
- Giggenbach W. F. (1984) Mass transfer in hydrothermal alteration systems – a conceptual approach. *Geochim. Cosmochim. Acta* **48**, 2693–2711.
- Giggenbach W. F. (1988) Geothermal solute equilibria. Derivation of Na–K–Mg–Ca geothermometers. *Geochim. Cosmochim. Acta* **52**, 2749–2765.
- Hedenquist J. W. (1990) The thermal and geochemical structure of the Broadlands-Ohaaki Geothermal System, New Zealand. *Geothermics* **19**, 151–185.
- Hedenquist J. W. and Lowenstern J. B. (1994) The role of magmas in the formation of hydrothermal ore deposits. *Nature* **370**, 519–527.
- Henley R. W. and Ellis A. J. (1983) Geothermal systems ancient and modern: a geochemical review. *Earth Sci. Rev.* **19**, 1–50.
- Hutcheon I., de Caritat P. and Abercrombie H. J. (1994) Clay minerals – equilibrium modes and temperature indicators. In *Alteration and Alteration Processes Associated with Ore-forming Systems* (ed. D. R. Lentz). Geological Association of Canada, Waterloo, Ontario, pp. 43–67.
- Inoue A. (1995) Formation of clay minerals in hydrothermal environments. In *Origin and Mineralogy of Clays: Clays and the Environment* (ed. B. Velde). Springer-Verlag, New York, pp. 245–329.
- Inoue A., Utada M. and Wakita K. (1992) Smectite-to-illite conversion in natural hydrothermal systems. *Appl. Clay Sci.* **7**, 131–145.
- Kaszuba J. P., Janecky D. R. and Snow M. G. (2005) Experimental evaluation of mixed fluid reactions between supercritical carbon

- dioxide and NaCl brine: relevance to the integrity of a geologic carbon repository. *Chem. Geol.* **217**, 277–293.
- Kaszuba J. P., Viswanathan H. S. and Carey J. W. (2011) Relative stability and significance of dawsonite and aluminum minerals in geologic carbon sequestration. *Geophys. Res. Lett.* **38**, L08404.
- Langmuir D. (1997) *Aqueous Environmental Chemistry*. Prentice Hall, Upper Saddle River, NJ.
- Lin H., Fujii T., Takisawa R., Takahashi T. and Hashida T. (2008) Experimental evaluation of interactions in supercritical CO₂/water/rock minerals system under geologic CO₂ sequestration conditions. *J. Mater. Sci.* **43**, 2307–2315.
- Liu L., Suto Y., Bignall G., Yamasaki N. and Hashida T. (2003) CO₂ injection to granite and sandstone in experimental rock/hot water systems. *Energy Convers. Manag.* **44**, 1399–1410.
- Lu P., Fu Q., Seyfried, Jr., W. E., Hedges S. W., Soong Y., Jones K. and Zhu C. (2013) Coupled alkali feldspar dissolution and secondary mineral precipitation in batch systems 2: new experiments with supercritical CO₂ and implications for carbon sequestration. *Appl. Geochem.* **30**, 75–90.
- Mahon W. A. J. (1966) Silica in hot water discharged from drillholes at Wairakei, New Zealand. *N. Z. J. Sci.* **9**, 135–144.
- Mahon W. A. J., Klyen L. E. and Rhode M. (1980) Neutral sodium/bicarbonate/sulphate hot waters in geothermal systems. *J. Jpn. Geotherm. Energy Assoc.* **17**, 11–24.
- Mandalaparty P., Deo M. and Moore J. (2011) Gas-compositional effects on mineralogical reactions in carbon dioxide sequestration. *SPE J.*, 949–958, SPE 124909.
- Massachusetts Institute of Technology (2006). The future of geothermal energy: impact of enhanced geothermal systems (EGS) on the United States in the 21st century: An assessment. Cambridge, MA.
- McPherson B. J. O. L. and Bredehoeft J. D. (2001) Overpressures in the Uinta basin, Utah: analysis using a three-dimensional basin evolution model. *Water Resour. Res.* **37**, 857–871.
- Moore J. N. and Simmons S. F. (2013) More power from below. *Science* **340**, 933–934.
- Mottl M. J. and Holland H. D. (1978) Chemical exchange during hydrothermal alteration of basalt by seawater – I. Experimental results for major and minor components of seawater. *Geochim. Cosmochim. Acta* **42**, 1103–1115.
- Naumov V. B., Dorofeev V. A. and Mironova O. F. (2011) Physicochemical parameters of the formation of hydrothermal deposits: A fluid inclusion study. I. Tin and tungsten deposits. *Geochem. Int.* **49**, 1002–1021.
- Nelson P. H. (1994) Permeability–porosity relationships in sedimentary rocks. *Log Anal.* **38–62**, 1994.
- Newell D. L., Kaszuba J. P., Viswanathan H. S., Pawar R. J. and Carpenter T. (2008) Significance of carbonate buffers in natural waters reacting with supercritical CO₂: Implications for monitoring, measuring and verification (MMV) of geologic carbon sequestration. *Geophys. Res. Lett.* **35**, L23403.
- Pan F., McPherson B. J., Lichtner P. C., Karra S., Lo Ré C., Kaszuba J. P., Lu C., and Xu T. (2012) Numerical simulations of interactions between supercritical CO₂ and high-temperature fractured rocks in enhanced geothermal systems. In *Proceedings: Thirty-Seventh Workshop on Geothermal Reservoir Engineering*. Stanford University, Palo Alto, CA. SGP-TR-194.
- Patrier P., Papapanagiotou P., Beaufort D., Traineau H., Bril H. and Rojas J. (1996) Role of permeability versus temperature in the distribution of the fine (<0.2 m) clay fraction in the Chipilapa geothermal system (El Salvador, Central America). *J. Volcanol. Geotherm. Res.* **72**, 101–120.
- Pruess K. (2006) Enhanced geothermal systems (EGS) using CO₂ as working fluid – a novel approach for generating renewable energy with simultaneous sequestration of carbon. *Geothermics* **35**, 351–367.
- Randolph J. B. and Saar M. O. (2011) Combining geothermal energy capture with geologic carbon dioxide sequestration. *Geophys. Res. Lett.* **38**, L10401. <http://dx.doi.org/10.1029/2011GL047265>.
- Reed M. H. (1997) Hydrothermal alteration and its relationship to ore fluid composition. In *Geochemistry of Hydrothermal Ore Deposits* (ed. H. L. Barnes). John Wiley & Sons, New York, pp. 303–365.
- Reyes A. G. and Cardile C. M. (1989) Characterization of clay scales forming in Phillipine geothermal wells. *Geothermics* **18**, 429–446.
- Rigault C., Patrier P. and Beaufort D. (2010) Clay minerals related to circulation of near neutral to weakly acidic fluids in active high energy geothermal systems. *Bull. Soc. Geol. Fr.* **181**, 337–347.
- Rimstidt J. D. (1997) Gangue mineral transport and deposition. In *Geochemistry of Hydrothermal Ore Deposits* (ed. H. L. Barnes). John Wiley & Sons, New York, pp. 487–516.
- Rimstidt J. D. and Barnes H. L. (1980) The kinetics of silica–water reactions. *Geochim. Cosmochim. Acta* **44**, 1683–1699.
- Rose A. W. and Burt D. M. (1979) Hydrothermal alteration. In *Geochemistry of Hydrothermal Ore Deposits* (ed. H. L. Barnes). John Wiley & Sons, New York, pp. 632–684.
- Rosenbauer R. J., Koksalan T. and Palandri J. L. (2005) Experimental investigation of CO₂–brine–rock interactions at elevated temperature and pressure: implications for CO₂ sequestration in deep-saline aquifers. *Fuel Process. Technol.* **86**, 1581–1597.
- Savage D., Cave M. R., Milodowski A. E. and George I. (1987) Hydrothermal alteration of granite by meteoric fluid: an example from the Carnmenellis Granite, United-Kingdom. *Contrib. Mineral. Petrol.* **96**, 391–405.
- Schiffman P. and Fridleifsson G. O. (1991) The smectite–chlorite transition in drillhole NJ-15, Nesjavellir geothermal field, Iceland: XRD, BSE and electron microprobe investigations. *J. Metamorphic Geol.* **9**, 679–696.
- Seyfried, Jr., W. E. and Bischoff J. L. (1977) Hydrothermal transport of heavy metals by seawater: the role of seawater/basalt ratio. *Earth Planet. Sc. Lett.* **34**, 71–77.
- Seyfried, Jr., W. E., Janecky D. R. and Berndt M. E. (1987) Rocking autoclaves for hydrothermal experiments, II. The flexible reaction-cell system. In *Hydrothermal Experimental Techniques* (eds. G. C. Ulmer and H. L. Barnes). John Wiley & Sons, New York, pp. 216–239.
- Simmons S. F. and Browne P. R. L. (2000) Hydrothermal minerals and precious metals in the Broadlands-Ohaaki Geothermal System: Implications for understanding low-sulfidation epithermal environments. *Econ. Geol.* **95**, 971–999.
- Steiner A. (1968) Clay minerals in hydrothermally altered rocks at Wairakei, New Zealand. *Clays Clay Min.* **16**, 193–213.
- Stumm W. and Morgan J. J. (1996) *Aquatic Chemistry: Chemical Equilibria and Rates in Natural Waters*. John Wiley & Sons, New York.
- Sun R. (2011) Personal email communication to Xiuyu Wang (University of Wyoming) regarding executable file for Duan & Sun, 2003. November 20.
- Suto Y., Liu L., Yamasaki N. and Hashida T. (2007) Initial behavior of granite in response to injection of CO₂-saturated fluid. *Appl. Geochem.* **22**, 202–218.
- Ueda A., Kato K., Oshumi T., Yajima T., Ito H., Kaieda H., Metcalfe R. and Takase H. (2005) Experimental studies of CO₂–rock interaction at elevated temperatures under hydrothermal conditions. *Geochem. J.* **39**, 417–425.

- Vidal O., Baldeyrou A., Beaufort D., Fritz B., Geoffroy N. and Lanson B. (2012) Experimental study of the stability and phase relations of clays at high temperatures in a thermal gradient. *Clays Clay Min.* **60**, 200–225.
- Wang Y. and Xu H. (2006) Geochemical chaos: periodic and nonperiodic growth of mixed-layer phyllosilicates. *Geochim. Cosmochim. Acta* **70**, 1995–2005.
- Ward S. H., Parry W. T., Nash W. P., Sill W. R., Cook K. L., Smith R. B., Chapman D. S., Brown F. H., Whelan J. A. and Bowman (1978) A summary of the geology, geochemistry, and geophysics of the Roosevelt Hot Springs thermal area, Utah. *Geophysics* **43**, 1515–1542.
- Whitney G. (1990) Role of water in the smectite-to-illite reaction. *Clays Clay Min.* **38**, 343–350.

Associate editor: Clark M. Johnson